REPORT DOCUMENTATION PAGE

1. AGENCY USE ONLY (Leave Blank)	2. REPORT DATE 4/24/02	3. REPORT TYPE AND DATES COVERED Final (05/01/97–01/31/02)

4. TITLE AND SUBTITLE

Passive and Active Control of Supersonic Axisymmetric Base Flows: Direct Numerical Simulations and Large-Eddy Simulations

5. FUNDING NUMBERS

DAAG 55-97-0128

6. AUTHOR(S)

Fasel, Hermann F.

7. PERFORMING ORGANIZATION NAME(S) AND ADDRESS(ES)

Department of Aerospace and Mechanical Engineering, University of Arizona, P.O. Box 210119, Tucson, AZ 85721-0119

8. PERFORMING ORGANIZATION REPORT NUMBER

9. SPONSORING / MONITORING AGENCY NAME(S) AND ADDRESS(ES)

U. S. Army Research Office
P.O. Box 12211
Research Triangle Park, NC 27709-2211

10. SPONSORING / MONITORING AGENCY REPORT NUMBER

36422.1-EG

11. SUPPLEMENTARY NOTES

The views, opinions and/or findings contained in this report are those of the author(s) and should not be construed as an official Department of the Army position, policy or decision, unless so designated by other documentation.

12 a. DISTRIBUTION / AVAILABILITY STATEMENT

Approved for public release; distribution unlimited.

12 b. DISTRIBUTION CODE

A new compressible Navier-Stokes code in cylindrical coordinates was developed for investigating axisymmetric wakes of bluff-based bodies in supersonic flows.
In this code, high-order compact finite differences derived for non-equidistant grids are employed and a new state-of-the-art axis treatment is incorporated. Additionally, the fully three-dimensional transport equations for turbulent kinetic energy and turbulent dissipation are implemented to enable (steady or unsteady) Reynolds Averaged Navier Stokes (RANS) simulations. Furthermore, a new "Flow Simulation Methodology" (FSM) was developed for computing complex compressible flows. The centerpiece of FSM is a strategy to provide the proper amount of modeling of the subgrid scales.
This is accomplished by a "contribution function" which locally and instantaneously compares the smallest relevant scales to the local grid size. The contribution function is designed such that it provides no modeling if the computation is locally well resolved so that the computation approaches a Direct Numerical Simulation (DNS) in the fine grid limit, or provides modeling of all scales in the coarse grid limit and thus approaches an unsteady RANS (URANS) calculation. In between these resolution limits, the contribution function adjusts the necessary modeling for the unresolved scales while the larger (resolved) scales are computed as in traditional Large Eddy Simulations (LES). Preliminary results have shown that the new high-order code has great advantages for supersonic base flow simulations and that calculations, in particular together with FSM, will allow simulations of supersonic baseflows at much higher Reynolds numbers than possible with conventional LES.

14. SUBJECT TERMS	15. NUMBER OF PAGES 115
	16. PRICE CODE

17. SECURITY CLASSIFICATION OR REPORT UNCLASSIFIED	18. SECURITY CLASSIFICATION ON THIS PAGE UNCLASSIFIED	19. SECURITY CLASSIFICATION OF ABSTRACT UNCLASSIFIED	20. LIMITATION OF ABSTRACT UL

Enclosure 1

20021017 068

Passive and Active Control of Supersonic Axisymmetric Base Flows: Direct Numerical Simulations and Large Eddy Simulations

Final Report

Hermann F. Fasel and Richard D. Sandberg

April 19, 2002

The University of Arizona

TABLE OF CONTENTS

TABLE OF CONTENTS — *Continued*

LIST OF FIGURES

LIST OF FIGURES — *Continued*

LIST OF FIGURES — *Continued*

LIST OF FIGURES — *Continued*

ABSTRACT[1]

A new compressible Navier-Stokes code in cylindrical coordinates was developed for investigating axisymmetric wakes of bluff-based bodies in supersonic flows. In this code, high-order compact finite differences derived for non-equidistant grids are employed and a new state-of-the-art axis treatment is incorporated. Additionally, the fully three-dimensional transport equations for turbulent kinetic energy and turbulent dissipation are implemented to enable (steady or unsteady) Reynolds Averaged Navier Stokes (RANS) simulations. Furthermore, a new "Flow Simulation Methodology" (FSM) was developed for computing complex compressible flows. The centerpiece of FSM is a strategy to provide the proper amount of modeling of the subgrid scales. This is accomplished by a "contribution function" which locally and instantaneously compares the smallest relevant scales to the local grid size. The contribution function is designed such that it provides no modeling if the computation is locally well resolved so that the computation approaches a Direct Numerical Simulation (DNS) in the fine grid limit, or provides modeling of all scales in the coarse grid limit and thus approaches an unsteady RANS (URANS) calculation. In between these resolution limits, the contribution function adjusts the necessary modeling for the unresolved scales while the larger (resolved) scales are computed as in traditional Large Eddy Simulations (LES). Preliminary results have shown that the new high-order code has great advantages for supersonic base flow simulations and that calculations, in particular together with FSM, will allow simulations of supersonic baseflows at much higher Reynolds numbers than possible with conventional LES.

---

[1]Upon recommendation from ARO, the scope of work was shifted from passive and active control of supersonic axisymmetric base flows towards development of a compact Navier-Stokes code in combination with a new Flow Simulation Methodology.

1. INTRODUCTION

For axisymmetric aerodynamic bodies in supersonic flight, the flow field in the wake region has considerable effect on the aerodynamic drag. Even small changes in the flow behavior of the wake may affect the performance of the entire flight vehicle, e.g., missiles, rockets, or projectiles. The effect of the wake on the aerodynamic drag is mainly due to the recirculation region that develops in the base region of the body and thus to the low pressure associated with the recirculating flow (base drag). Flight tests with projectiles (U.S. Army 549 projectile) have shown that the base drag may account for up to 35% of the total drag (see Rollstin, 1987). This suggests that attempts to modify the near wake flow such that the base pressure would increase could be highly rewarding with respect to drag reduction and, as a consequence, with regard to increasing the performance characteristics of flight vehicles or projectiles. However, in order to modify the near-wake flow effectively, a detailed understanding of the underlying physical mechanisms that are responsible for the flow behavior is required.

For this reason, in the past, numerous research efforts, experimental, theoretical, and computational, have focused on understanding the physics of the base flow or the near-wake region. However, due to the difficulty of the problem and limitations of experimental and numerical techniques, these

studies focused almost exclusively on the mean flow behavior and not on the potential effects of the unsteady structures of the turbulent flow. As discussed below, if energetic (coherent) structures are indeed present in such flows, and more recent evidence indicates that they are [see Smith & Dutton (1996), Bourdon & Dutton (1998), Harris & Fasel (1996), and Tourbier & Fasel (1994)], the dynamical behavior of such structures may have a profound effect on the resulting mean flows. Also, as a consequence of this, profound modifications of the base flow behavior and thus the base drag must involve a modification of the dynamics of these large structures.

In recent years, techniques for reducing the base drag have been suggested and investigated, such as boattailing, base bleed, base burning, etc. [see, for example, Sahu *et al.* (1985), Nietubicz & Gibeling (1993), Sahu & Heavey (1995), Sahu & Nietubicz (1994), Mathur & Dutton (1996a,b) and Bourdon & Dutton (2000a)]. Such techniques can indeed modify the mean base flow and, as a consequence, the base drag. However, the underlying mechanisms responsible for the changes are not understood. In order to optimize such techniques for practical applications, it is essential that the fundamental mechanisms that are responsible for these changes are brought to light. As discussed below, the key to uncovering these essential mechanisms is in first understanding the role of the (coherent) turbulent flow structures and, in particular, how the dynamics of these structures is influenced by proposed

techniques for drag reduction.

1.1 Experimental Research

Historically, the fundamentals of the near-wake behavior were first investigated using experiments almost exclusively. However, wind tunnel experiments suffered from the difficulty of properly supporting the (axisymmetric) base model so as not to cause undue effects on the flow field behind the base Chapman (1951). In experimental investigations, different methods of model support have been proposed; for example, rear sting support Donaldson (1955), side mounted struts Chapman (1951), and up stream wire mounts Dayman (1963). However, all of these techniques have shown non negligible effects on the near wake behavior and, in particular, on the base pressure. The forward sting support used by Herrin & Dutton (1991) and also in subsequent and current experimental investigations appears to be superior to other methods with regard to minimizing flow interference [also see Dutton & Addy (1993), Herrin & Dutton (1995), Herrin & Dutton (1994), Mathur & Dutton (1996a), Mathur & Dutton (1996b) and Bourdon & Dutton (1998, 2000a)].

In addition to the interference caused by model support, wind tunnel interference can have a considerable influence on the base flow behavior. Therefore, extra care has to be taken in order to understand and minimize the

effects of vibrations, upstream sound, noise radiated from turbulent boundary layers of the wind tunnel walls, blockage, etc. This is particularly important for investigating the role of large coherent structures and for reliably testing passive control techniques (see section 2.2). For the wake flow with a central jet (power on mode), wind tunnel interference would be somewhat less of a problem and therefore appears to be experimentally easier. However, for this case, the shear layers become much thinner, making it much harder to resolve the resulting large gradients when taking measurements.

Furthermore, the quality of experimentally obtained flow data in the wake is often compromised whenever intrusive probes (such as Pitot pressure tubes, hot wire probes, etc.) are used. This is particularly true for measurements within the recirculating region immediately downstream of the blunt base of the body. The strong sensitivity to intrusive probes is due to the absolute/global instability that may be present in supersonic wake flows (see section 2.2). Absolute stability behavior is very sensitive to small changes of the mean flow velocity profiles, in particular when solid surfaces (probes) are inserted, which can change the upstream pressure feedback mechanism.

In free-flight experiments, many of the above mentioned difficulties do not arise. However, in addition to the much greater cost, free flight experiments also suffer from major disadvantages. For example, it is not possible to map out details of the flow field as is possible with wind tunnel experiments.

Also, the reliability of flight test data is often in question because of the considerable difficulties in controlling conditions and parameters in the free flight tests.

In recent years, many experimental efforts have focused on modifying the base flow in order to reduce the base drag. So far, only so-called passive control methods have been considered, such as boattailing, base bleed, and base burning [see, for example, Cortwright & Schroeder (1951), Reid & Hastings (1959), Bowman & Clayden (1968), Clayden & Bowman (1968), Valentine & Przirembel (1970), Hubbartt *et al.* (1981), Ding *et al.* (1992), Mathur & Dutton (1996*a,b*)]. These experiments have shown that there are potentially considerable rewards for passive flow control. However, it is still not understood why certain measures are more effective than others (or why others do not work at all) and what the optimal parameters should be. The reason for this is that the fundamental physical mechanisms in a supersonic wake flow are not yet understood.

1.2   Numerical Simulations

Because of the difficulties and uncertainties associated with experiments, researchers have looked to numerical simulations as attractive alternatives and/or complements to experimental investigations. Sparked by the rapid increase in the computing power of supercomputers in the last two decades,

numerous attempts were made to calculate the flow field around and behind axisymmetric bodies aligned with the free stream. In numerical simulations, problems associated with wind tunnel interference, model support, probe intrusion, etc., are not present. In addition to possibly providing further understanding of the relevant physics involved, these calculations were motivated by the considerable challenge that this complicated flow field provides for computational fluid dynamicists. The computational challenge arises mainly from the combination of shock waves, thin free shear layers, boundary layers, and recirculating regions; associated with this are highly disparate length scales and local regions of very high gradients. Reliable and realistic computations can therefore only be performed if the high gradients can be adequately resolved.

Furthermore, the wake flow is turbulent (or at least transitional), requiring adequate turbulence models. In practically all earlier and in most of the more recent numerical attempts, only the steady flow field has been calculated. In these computations, "Reynolds Averaged Navier Stokes"(RANS) formulations were used in combination with a turbulence model, such as the algebraic eddy viscosity model of Baldwin and Lomax, the two equation $K - \varepsilon$ model, or the $K - \omega$ model. In the literature, numerous attempts have been reported on calculating turbulent wake flows using either the complete Navier Stokes equations or the thin layer (parabolized) Navier Stokes

equations, or combinations thereof [for example, the parabolized equations in part of the flow field (typically up to the trailing edge of the body) and the full equations in another part (typically in the wake region)]. Also, variable (adaptive) grids were used in the computations in order to resolve the local large gradients of the flow field.

Relatively few direct comparisons of numerical simulations with laboratory experiments were attempted in the past. The more successful numerical calculations were able to capture the qualitative features of the experimentally obtained flow field. However, relevant quantities, such as turbulent shear stresses and, in particular, such fundamental aspects as the all important base pressure or the size of the separation bubble (recirculation region), were often not predicted well [see Petrie & Walker (1985)]. Also, and particularly disturbing, using different turbulence models but otherwise identical codes yielded inconsistent (and often contradictory) results. This is an indication that something fundamental might be amiss.

Childs & Caruso (1987) surveyed existing computational Navier Stokes methods for calculating turbulent compressible wake flows. They suggested that inadequate numerical resolution of the large gradients and, in particular, the turbulence modeling may be the major culprits for not being able to reliably and accurately calculate the flow field. It appears that because of the strong effect of different turbulence models on the results, even the

qualitative agreement between various computations and experiments may often have been entirely fortuitous. Similar observations were made by Sahu & Nietubicz (1994), who investigated the influence of different turbulence models for RANS calculations of supersonic axisymmetric base flows. They showed that, while some flow quantities can be modeled adequately by adjusting certain parameters in the turbulence model, other quantities do not agree well with experimental results.

Although considerable progress has been made in past years in using RANS calculations for supersonic axisymmetric wake flows behind missile type bodies, there is still no true reconciliation between experimental and computational results [see Delery & Wagner (1990)]. In addition to possible shortcomings of the numerical codes, the discrepancies were due in part to a lack of reliable experimental data, in particular due to a lack of experimental data in sufficient detail to allow scrutinizing comparisons between experiments and calculations. Now, due to the extensive experimental effort at the University of Illinois by Dutton and co-workers, sufficient and reliable experimental data are being made available for close comparison with numerical computations.

In spite of the discussed shortcomings of the Reynolds-averaged calculations, recent applications have attacked increasingly more difficult situations. As modification of wake flows is now being considered as a means of drag

reduction, RANS calculations have been performed to investigate, for example, the effects of base bleed [see, for example, Sahu *et al.* (1985), Sahu & Heavey (1995) and Danberg & Nietubicz (1992)] and base burning Nietubicz & Gibeling (1993). The simulations show a correct trend for the drag reduction when compared with experimental results. However, in some cases, even global flow field characteristics such as the centerline velocity are not in good agreement with experiments. This is an indication that certain mechanisms are difficult to model in RANS calculations. From the experimental effort of Dutton and co-workers, it is becoming increasingly more obvious that attempts to only calculate the steady flow might miss the essential physical mechanisms that are responsible for the base flow behavior. Dutton and co-workers have identified a significant time-dependent behavior and found large coherent structures that may play crucial roles in the base drag. These findings may be particularly important when modifications of the flow are attempted (for example, using boattailing, base bleed, etc.). Therefore, in order for numerical simulations to be useful for uncovering mechanisms relevant to the base drag in supersonic flows, they have to be able to capture the unsteady behavior resulting from the dynamics of the large (coherent) turbulent flow structures (see discussion section 2.2).

Another approach of turbulence modelling are Large Eddy Simulations (LES). For LES, only the large scale motion is computed directly. The sub-

grid scale structures which are assumed to be isotropic are modelled. This method was initially proposed by Smagorinsky (1963) who based his model on the Boussinesq assumption (Boussinesq (1877)) which states that the turbulent stresses can be related linearly to the mean velocity gradients by an eddy viscosity.

For the flow under consideration, LES would be the method of choice because of the ability to capture three-dimensional and unsteady effects. The shortcomings of the standard Smagorinsky LES model which include the failure to account for normal stresses (which are present in the recirculation region for example), an ad-hoc constant that is only valid for a certain flow region and "damping functions that are needed at the walls which are empirical in nature and do not apply to general wall bounded turbulent flows" (Speziale (1997)) make this model ill-suited for this research. Further shortcomings of this widely used model can also be found in Jiménez & Moser (1998).

In the last few years, a new class of hybrid RANS/LES turbulence models has emerged that tries to unify the best of both worlds. The underlying principle is to conduct a RANS type simulation close to a wall and perform an LES away from the wall to capture the unsteadiness. One way of implementing this method has been proposed by Spalart *et al.* (1997) and is known as Detached Eddy Simulation (DES). In principle, the method compares the

distance to the closest wall with the product of the local grid spacing and an empirical constant. For small distances, the eddy viscosity is computed according to a one-equation RANS model, otherwise a Smagorinsky type LES is computed.

This model has been applied to the experimental case of Dutton and co-workers by Forsythe & Hoffmann (2000) who mainly explored different choices for the empirical constant. The mean flow quantities in the recirculation region were found to deviate significantly from the experiments, even though they reported very good agreement of the mean base pressure distribution. Later work by Forsythe *et al.* (2002) incorporated the compressible shear layer corrections into the RANS-part of the simulation and it was shown that this modification had a negligible impact on the solution.

Another methodology is based on using the same turbulence model in both limits and smoothly blend from an LES to a RANS. This is achieved by a contribution function which locally determines how much of the turbulence is resolved by the computational grid. This new Flow Simulation Methodology (FSM) was proposed by Speziale and Fasel (see Speziale (1998), Sandberg (1999), Zhang *et al.* (2000) and recently extended to compressible flows by Terzi & Fasel (2002)). The turbulence model is a state-of-the-art explicit algebraic Reynolds stress model (ASM) developed by Gatski & Speziale (1993), which is derived from the full Reynolds transport equations. It features an

anisotropic eddy viscosity with strain dependent coefficients and accounts for normal stresses and rotational effects.

The contribution function is determined by comparing the local grid size with a local estimate of an appropriate turbulent length scale, usually chosen to be the Kolmogorov length scale (L_K). For very coarse grids (compared to L_K), the Reynolds stress from the turbulence model is scaled with unity and a RANS simulation is conducted (Note that the ASM is capable of capturing unsteadiness, therefore an unsteady RANS (URANS) simulation is performed). In the limit of fine resolution, the Reynolds stress is multiplied with zero, recovering a DNS. Between these two limits, a "non-traditional" LES based on the nonlinear ASM is performed. This new methodology seems to be very promising for the flow under investigation as it will enable to capture the relevant large structures and should therefore be able to predict the mean flow quantities in the near-wake region.

Towards this end, we initiated several years ago (with funding from ARO) a computational program that exactly addresses these issues [see Tourbier & Fasel (1994), Tourbier (1996), and Harris & Fasel (1996)]. We believe that high-quality Direct Numerical Simulations (DNS), Large-Eddy Simulations (LES), unsteady RANS simulations (URANS) and especially FSM are required to uncover the essential physics and, equally important, due to the complexity and difficulties in experiments and simulations as discussed

above, that these simulations are carried out simultaneously and in close collaboration with experiments.

2.   TECHNICAL BACKGROUND

2.1   Mean Flow Field Behind a Cylindrical Body with a Blunt Base

The mean flow field for the near wake region downstream of an axisymmetric body with a blunt base is shown schematically in figure 2.1. This flow topology is based on the experiments by Dutton and co-workers Herrin & Dutton (1994). This mean flow field, shown in figure 2.1, disguises the fact that the flow is turbulent and highly unsteady. However, even the mean-flow topology is already very complex: Downstream of the expansion waves emanating from the sharp corner, a thin, yet very energetic shear layer develops that encloses a massively separated (recirculation) region with a rear stagnation point. The shear layer divides the flow field into a high-speed supersonic outer region and a low-speed region near the base. Downstream of the rear stagnation point, recompression occurs and the flow field from there on looks increasingly like that of a subsonic wake at several diameters from the base. The behavior in the separated (recirculation) region has a considerable influence on the base drag, yet this region is strongly dependent on the topology of the shear layer and the ensuing recompression region. The sharp radial gradients in the shear layer and the rapid spatial changes make the flow field highly complex, and it is therefore very difficult to investigate

both experimentally and computationally, even if the flow field were steady.

However, as mentioned, the mean flow topology of Figure 2.1 is misleading
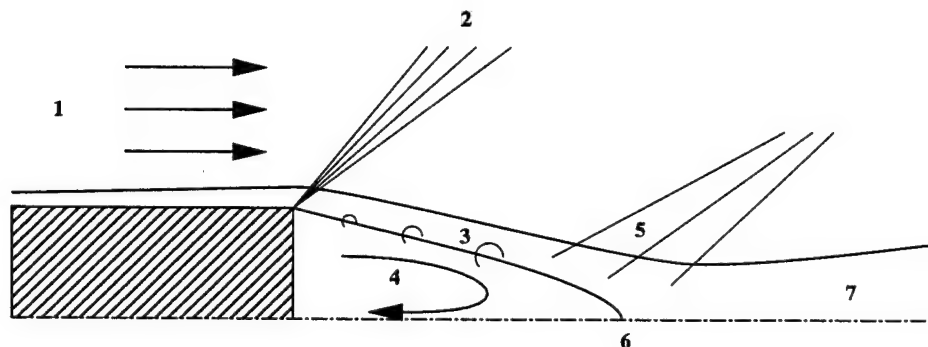
Figure 2.1 Schematic of flow field behind a cylindrical body with a blunt base (mean flow).

and disguises the fact that, in reality, the flow is *highly* unsteady, caused by the very energetic shear layers, the flow recirculation, and rapid downstream adjustment in the recompression region.

Dutton and co-workers have started to document the unsteady nature of this flow and have found that, even in the dead-air region, significant dynamical behavior of the flow can be observed with velocities up to 100 m/s (Herrin & Dutton (1994)). The strong dynamical behavior in the (mean) recirculating region was also studied in detail using our computational tools [Tourbier & Fasel (1994), Harris & Fasel (1996); see also section 6]. The question is, of course, how relevant the unsteady nature of the flow is to the performance of projectiles and missiles.

2.2   Large-Scale Coherent Structures

It is well known that for subsonic (incompressible) wakes, the dynamics of the large (coherent) structures play a dominant role in the local and global behavior of the flow. This evidence was found from both experimental investigations and numerical simulations (including ours) and was confirmed by theoretical studies. For incompressible bluff body wakes, it has been well established that the existence of absolute and global instabilities is responsible for the development of the large structures (Huerre & Monkewitz (1990)). Using numerical simulations, absolute/global instabilities were found for a two-dimensional bluff body with a blunt base by Hannemann & Oertel (1989) and for an axisymmetric body with a blunt base by Schwarz *et al.* (1994). The absolutely/globally unstable modes for the axisymmetric base flow are of a helical nature.

For supersonic speeds, on the other hand, relatively little is known about the dynamical behavior of the large structures in turbulent flows or, in particular, if absolute/global instabilities exist. This is true for supersonic flows in general and for axisymmetric wakes in particular. The explanation for this void is that experiments are difficult to conduct for supersonic speeds (see discussion in introduction). In addition, expensive facilities and intricate diagnostic equipment are required for supersonic hydrodynamic stability

experiments.

Due to the lack of guidance from experimental investigations prior to our computational research initiative on the subject, no successful computational/theoretical attempts have been made to study the unsteady, dynamical behavior of transitional or turbulent supersonic axisymmetric base flows. We feel that, as for subsonic wakes, it is exactly the dynamical behavior of the large scale structures that strongly influences the flow field in supersonic axisymmetric wakes. We conjecture that the discrepancies between experiments and steady Reynolds averaged Navier Stokes calculations may be due to the fact that this unsteady, dynamic behavior of the large scale structures is not properly accounted for in current turbulence models. The fact that the results of Reynolds averaged calculations depend strongly on the turbulence models used [see Petrie & Walker (1985) and Sahu (1992)] supports this conjecture.

As in the subsonic case, supersonic wake flows behind a blunt base are dominated by a separated region, and associated with it is (in the mean) an axisymmetric shear layer originating from the sharp corner of the base. Turbulent, subsonic (incompressible) shear layers are characteristic of developing large coherent structures that are of a highly unsteady nature. (For two dimensional shear layers, these large structures are strongly two-dimensionally organized.) Thus, it is not surprising that large coherent structures, which

can be observed to originate in the shear layers directly behind the blunt base, are present also for subsonic turbulent wakes behind blunt trailing edges.

There is considerable evidence that the cause of the large structures is due to the hydrodynamic instability of the (time-averaged) mean flow and that the development of these structures can be captured by *stability theory*. In fact, certain aspects of the development can be captured even with *linear stability theory* although intensities (amplitudes) of the structures are often too large for the linear stability theory to be valid. Experimental results for incompressible turbulent mixing layers, two-dimensional turbulent wakes, and axisymmetric wakes with a blunt base and comparison with linear stability theory have shown that certain key features, such as dominant frequencies, mode shapes (amplitude distributions), and streamwise spacing (streamwise wave lengths) of the structures can be well predicted by linear stability theory (Wygnanski *et al.* (1986), Marasli *et al.* (1989)). These investigations support the notion that hydrodynamic instabilities give rise to the generation and development of large structures.

The dynamical behavior of these structures is responsible for the strong unsteady flow behavior in the wake. Thus, in reality, there is no steady turbulent wake flow (and, in particular, there is no dead wake region near the base of a bluff body), even when the small scale (high frequency) fluctuations are not taken into consideration. Rather, the flow is highly unsteady,

dominated by large amplitude and, relative to the small scales, low frequency fluctuations. The steady mean flow measured in experiments is in fact the time average of the time dependent fluctuating flow field. Since the amplitude of these large scale fluctuations can be relatively large, the total flow field cannot actually be composed by linear superposition of the various fluctuating components onto the (steady) mean flow field. Rather, because of nonlinear interaction between the various fluctuation components, the actual mean flow may be strongly dependent on the composition of the fluctuating parts of the flow field.

This evidence was confirmed experimentally for incompressible wake flows Wygnanski et al. (1986), Marasli et al. (1989) by artificially forcing the flow. With artificial forcing, existing modes (structures) could be modified or new modes (structures) created. As a consequence, the mean flow could be modified substantially. This study showed convincingly that there is no unique turbulent mean flow for the wake and not even for the far wake. Rather, the mean (steady) wake flow is strongly dependent on the nature of the large-scale coherent structures and, as a consequence, on their dynamical behavior.

With this in mind, it is not surprising that mean flow fields depend strongly on experimental conditions and can even vary for the same facility with minor changes of the experimental parameters. Also, for this reason, it is not surprising that current turbulence models for calculating mean

flows using the Reynolds averaged Navier Stokes formulations are performing poorly for flows that are known to be dominated by the dynamics of large structures, that is, for flows with massive separations and free shear layers. Chances to arrive at better turbulence models are rather slim unless the physical and dynamical behavior of the large structures are better understood and until this knowledge can be implemented in the turbulence modeling.

Thus, in the context of the proposed research, the question arises: Do large structures play a similarly important role for supersonic separated flows and in particular for supersonic axisymmetric wakes? Unfortunately, there are relatively few experimental investigations that have focused on this issue. However, when looking at flow visualization pictures of supersonic wake flows, very distinct patterns with large scale structures can be observed.

For planar supersonic shear layers, the experimental investigations of Papamoschou & Roshko (1988) have convincingly demonstrated the presence of dominant large scale structures for a variety of conditions, e.g., Mach numbers and density ratios. In fact, relative to the shear layer thickness, these structures are often considerably larger (and therefore appear to be more dominant) than those for incompressible shear layers. Large scale (coherent) structures for supersonic shear layers were also observed by Ortwerth & Shine (1977) and for supersonic jets by Oertel (1979). For the supersonic ax-

isymmetric shear layer behind a backward-facing step investigated by Roshko & Thomke (1966), flow visualization suggests a mean flow that is predominantly periodic in the azimuthal direction, indicating possibly the presence of large (coherent) structures with a dominant azimuthal wave length [see Figure 6 in Roshko & Thomke (1966)].

The fact that wind tunnel interference and interference from model support are strongly affecting the mean flow behavior for supersonic axisymmetric wake flow experiments may be an indication that this might be caused by the presence of large coherent structures. The dynamical behavior of the large structures may be changed by the interference disturbances, or additional large structures may be generated due to changes in the hydrodynamic stability behavior of the mean flow, as discussed above.

Some quantitative evidence of the existence of dominant large structures in supersonic axisymmetric wake flows was provided by the experiments of Demetriades (1968), who investigated the unsteady nature of the flow field. The amplitude spectra (see Figures 11 to 14 in Demetriades) display distinct peaks at certain (relatively low) frequencies, thus indicating the presence of dominant modes (structures). This is supported by plots of rms-amplitude distributions (with respect to radial distance from the centerline) for the axial velocity fluctuation and the density fluctuation (Figures 2 and 3, respectively, of Demetriades). The amplitude distribution for the velocity fluctuation is

highly reminiscent of that of an incompressible axisymmetric wake, where it is known that this profile is due to the presence of dominant, large coherent structures (Cannon & Champagne (1991)). In fact, Morkovin (1968) suggested long ago that when normalized properly, the distribution of fluctuations (as caused by large structures) has a universal character, even in very diverse flow regimes, e.g., even when comparing subsonic and supersonic flows.

In a well-planned and carefully executed experimental program at the University of Illinois, Dutton and co-workers [see, e.g., Smith & Dutton (1996)] identified coherent structures for a supersonic two-dimensional wake behind a blunt base. The observed dominant structures appear to be significant relative to the shear layer thicknesses. These observations were in qualitative agreement with those of Papamoschou & Roshko (1988) for a planar supersonic shear layer. From our previous numerical investigations of transitional and turbulent base flows (two-dimensional and axisymmetric; albeit at lower Reynolds numbers than the experiments, see section 5), we found highly energetic structures with amplitudes of about 15% of the free stream velocity that may have a significant effect on the global flow behavior (see earlier discussion).

More recently, employing sophisticated flow visualization techniques, Dutton and co-workers (Bourdon & Dutton (1998, 2000b)) were able to clearly

show the presence of large turbulence structures in the axisymmetric base flow. Therefore, from our previous simulations and the recent experiments by Dutton and co-workers, we have sufficient evidence that large coherent structures are present in supersonic axisymmetric base flows and may indeed play an important role. The fact that dominant structures can exist in axisymmetric wake flows and may play an important role is crucial to the proposed research, as numerical simulations will be employed for these investigations. For numerical simulations to be useful for providing new insight into the physics of supersonic base flows, it is therefore essential that the simulation techniques are such that the role of the large turbulent structures is accurately represented and the dynamics of the structures can be captured reliably.

3. GOVERNING EQUATIONS

The flow is assumed to be an ideal gas with constant specific heat coefficients and the following assumptions are made for the constitutive relations: the flow can be treated as a Newtonian fluid with zero bulk viscosity, the Fourier law is valid for heat conduction, the Prandtl number is constant in the region of interest and the viscosity can be evaluated according to Sutherland's law.

3.1 Dimensional Equations

The governing field equations for this research are the three-dimensional compressible Navier-Stokes equations in cylindrical coordinates. Body forces are neglected and the Prandtl number is assumed constant. The conservative form of the equations was chosen because it can be put in vector form. This method was used by Thumm (1991) and is described in Anderson *et al.* (1984). Following are the equations in tensor notation, with an asterisk denoting a dimensional variable.

Continuity:

$$\rho^*_{,t^*} + \left(\rho^* u_k^*\right)_{,k^*} = 0 \tag{3.1}$$

Momentum:

$$\left(\rho^* u_i^*\right)_{,t^*} + \left(\rho^* u_i^* u_k^* + p^* \delta_{ik} - \tau_{ik}^*\right)_{,k^*} = 0 \tag{3.2}$$

Total energy:

$$\left(\rho^* E^*\right)_{,t^*} + \left(\rho^* u_k^* H^* + q_k^* - \tau_{ik}^* u_i^*\right)_{,k^*} = 0 \tag{3.3}$$

where the total energy and the total enthalpy are

$$E^* = c_v^* T^* + \frac{1}{2} u_j^* u_j^* \quad \text{and} \quad H^* = E^* + \frac{p^*}{\rho^*} \quad , \text{respectively.} \tag{3.4}$$

The stress tensor is

$$\tau_{ik}^* = 2\mu^* S_{ik}^* - \frac{2}{3}\mu^* S_{jj}^* \delta_{ik} \quad \text{with} \quad S_{ik}^* = \frac{1}{2}\left(u_{i,k^*}^* + u_{k,i^*}^*\right) \tag{3.5}$$

and the heat flux vector

$$q_k^* = -\kappa^* T_{,k^*}^* \,. \tag{3.6}$$

Finally, the equation of state closes the system and is given as

$$p^* = \rho^* \mathcal{R}^* T^* \,. \tag{3.7}$$

Sutherland's Law is used to calculate the viscosity:

$$\frac{\mu^*}{\mu_0^*} = \left(\frac{T^*}{T_0^*}\right)^{\frac{3}{2}} \left(\frac{T_0^* + \mathcal{R}_{Su}^*}{T^* + \mathcal{R}_{Su}^*}\right) \tag{3.8}$$

with

$$\mathcal{R}_{Su}^* = 110.6K \tag{3.9}$$

3.2 Non-dimensional Equations

All quantities are made dimensionless by conditions at a reference point in the flow, which in this case is the freestream/inflow point, and a reference

length, which will be chosen to be the body radius. All field equations and constitutive relations are made dimensionless via the set $T_\infty^*, u_\infty^*, \rho_\infty^*, r^*, \mu_\infty^*, \kappa_\infty^*$. This leads to the following dimensionless groups:

$$Re = \frac{\rho_\infty^* u_\infty^* r^*}{\mu_\infty^*} \;,\; Pr = \frac{\mu_\infty^* c_p^*}{\kappa_\infty^*}$$

$$Ec = \frac{u_\infty^{*2}}{c_p^* T_\infty^*} \quad,\quad M_\infty = \frac{u_\infty^*}{a_\infty^*} \tag{3.10}$$

The mass, momentum and energy equations are made dimensionless by multiplying by $r^*/\rho_\infty^* u_\infty^*$, $r^*/\rho_\infty^* u_\infty^{*2}$, and $r^*/\rho_\infty^* u_\infty^{*3}$, respectively. This leads to the non-dimensional equations, now given in vector form in cylindrical coordinates.

$$\frac{\partial U}{\partial t} + \frac{\partial A}{\partial z} + \frac{\partial B}{\partial r} + \frac{1}{r}\frac{\partial C}{\partial \theta} + \frac{1}{r}D = 0 \tag{3.11}$$

with

$$U = \begin{pmatrix} \rho \\ \rho u \\ \rho v \\ \rho w \\ \rho E \end{pmatrix} \tag{3.12}$$

$$A = \begin{pmatrix} \rho u \\ \rho u^2 + p - \tau_{zz} \\ \rho uv - \tau_{rz} \\ \rho uw - \tau_{\theta z} \\ \rho uH + q_z - u\tau_{zz} - v\tau_{rz} - w\tau_{\theta z} \end{pmatrix} \tag{3.13}$$

$$B = \begin{pmatrix} \rho v \\ \rho uv - \tau_{rz} \\ \rho v^2 + p - \tau_{rr} \\ \rho vw - \tau_{r\theta} \\ \rho vH + q_r - u\tau_{rz} - v\tau_{rr} - w\tau_{r\theta} \end{pmatrix} \tag{3.14}$$

$$
C = \begin{pmatrix} \rho w \\ \rho u w - \tau_{\theta z} \\ \rho v w - \tau_{r\ theta} \\ \rho w^2 + p - \tau_{\theta\theta} \\ \rho w H + q_\theta - u\tau_{\theta z} - v\tau_{r\theta} - w\tau_{\theta\theta} \end{pmatrix} \tag{3.15}
$$

$$
D = \begin{pmatrix} \rho v \\ \rho u v - \tau_{rz} \\ \rho v^2 - \rho w^2 - \tau_{rr} + \tau_{\theta\theta} \\ 2\rho v w - 2\tau_{r\theta} \\ \rho v H + q_r - u\tau_{rz} - v\tau_{rr} - w\tau_{r\theta} \end{pmatrix} \tag{3.16}
$$

with the stress components

$$
\tau_{zz} = \frac{1}{Re}\left[2\mu S_{zz} - \frac{2}{3}\mu\left(S_{zz} + S_{rr} + S_{\theta\theta}\right) \right] \tag{3.17}
$$

$$
\tau_{rr} = \frac{1}{Re}\left[2\mu S_{rr} - \frac{2}{3}\mu\left(S_{zz} + S_{rr} + S_{\theta\theta}\right) \right] \tag{3.18}
$$

$$
\tau_{\theta\theta} = \frac{1}{Re}\left[2\mu S_{\theta\theta} - \frac{2}{3}\mu\left(S_{zz} + S_{rr} + S_{\theta\theta}\right) \right] \tag{3.19}
$$

$$
\tau_{rz} = \frac{1}{Re}2\mu S_{rz} \tag{3.20}
$$

$$
\tau_{\theta z} = \frac{1}{Re}2\mu S_{\theta z} \tag{3.21}
$$

$$
\tau_{r\theta} = \frac{1}{Re}2\mu S_{r\theta} \, . \tag{3.22}
$$

The strainrates in cylindrical coordinates are:

$$
S_{zz} = \frac{\partial u}{\partial z} \, , \ S_{rr} = \frac{\partial v}{\partial r} \, , \ S_{\theta\theta} = \frac{1}{r}\frac{\partial w}{\partial \theta} + \frac{v}{r} \, , \tag{3.23}
$$

$$
S_{rz} = \frac{1}{2}\left(\frac{\partial u}{\partial r} + \frac{\partial v}{\partial z} \right) \, , \ S_{\theta z} = \frac{1}{2}\left(\frac{\partial w}{\partial z} + \frac{1}{r}\frac{\partial u}{\partial \theta} \right) \quad \text{and} \quad S_{\theta r} = \frac{1}{2}\left(\frac{1}{r}\frac{\partial v}{\partial \theta} + r\frac{\partial}{\partial r}\frac{w}{r} \right) \, . \tag{3.24}
$$

Non-dimensionalizing Sutherland's Law yields

$$\mu\left(T\right) = T^{\frac{3}{2}}\left(\frac{1+\mathcal{R}_{Su}}{T+\mathcal{R}_{Su}}\right) \tag{3.25}$$

Note that since the Prandtl number is assumed constant throughout the flow field, the dimensionless thermal conductivity and viscosity are identical:

$$\mu = \frac{\mu^*}{\mu_\infty^*} = \left(\frac{\mu^*c_p^*}{\kappa^*}\right)\frac{\kappa^*}{\mu_\infty^*c_p^*} = (Pr)\frac{\kappa^*}{\mu_\infty^*c_p^*} = \left(\frac{\mu_\infty^*c_p^*}{\kappa_\infty^*}\right)\frac{\kappa^*}{\mu_\infty^*c_p^*} = \frac{\kappa^*}{\kappa_\infty^*} = \kappa \tag{3.26}$$

3.3 Averaged Equations

Following Speziale (1997), applying a filter to the governing equations, the fundamental equations for LES are found:

the filtered continuity equation

$$\frac{\partial\overline{\rho}}{\partial t} + \frac{\partial}{\partial x_k}\left(\overline{\rho}\widetilde{u}_k\right) \quad, \tag{3.27}$$

the filtered momentum equations

$$\frac{\partial}{\partial t}\left(\overline{\rho}\widetilde{u}_i\right) + \frac{\partial}{\partial x_k}\left[\overline{\rho}\widetilde{u}_i\widetilde{u}_k + \overline{p}\delta_{ik} - \left(\overline{\tau}_{ik} - \overline{\rho}\sigma_{ik}\right)\right] = 0 \quad, \tag{3.28}$$

and the resolved energy equation

$$\frac{\partial}{\partial t}\left(\overline{\rho}E_R\right) + \frac{\partial}{\partial x_k}\left[\overline{\rho}\widetilde{u}_k H_R + \overline{q}_k + Q_k - \widetilde{u}_i\left(\overline{\tau}_{ik} - \overline{\rho}\sigma_{ik}\right)\right] = \Pi \,, \tag{3.29}$$

where the overbar represents a standard filter (i.e., for this research, the implicit filter inherent to the discretization scheme with a filter width related to the grid size) and a tilde denotes the Favre-average defined as

$$\widetilde{f} = \frac{\overline{\rho f}}{\overline{\rho}} . \tag{3.30}$$

The velocity vector u_i and the temperature T are decomposed into a Favre-average and a fluctuating part (denoted by ") and the pressure p and the density ρ are split into the Reynolds-average (denoted by -) and a fluctuating part (denoted by ').

The resolved energy E, the resolved total enthalpy H, the resolved heat flux vector q_k and the resolved stress tensor $\overline{\tau}_{ik}$ are

$$E = c_v \widetilde{T} + \frac{1}{2} \widetilde{u}_j \widetilde{u}_j \quad , \quad H = E + \frac{\overline{p}}{\overline{\rho}} \quad , \quad \overline{q}_k = -\kappa \left(\frac{1}{PrEcRe} \right) \widetilde{T}_{,k} \quad , \tag{3.31}$$

$$\overline{\tau}_{ik} = \frac{2}{Re} \mu \left(\widetilde{S}_{ik} - \frac{1}{3} \widetilde{S}_{jj} \delta_{ik} \right) \quad \text{with} \quad \widetilde{S}_{ik} = \frac{1}{2} \left(\widetilde{u}_{i,k} + \widetilde{u}_{k,i} \right) , \tag{3.32}$$

respectively. The resolved molecular viscosity $\overline{\mu}$ is computed according to Sutherland's law (see e.g. White (1991))

$$\mu \left(\widetilde{T} \right) = \kappa \left(\widetilde{T} \right) = \widetilde{T}^{\frac{3}{2}} \left(\frac{1 + \mathcal{R}_{Su}}{\widetilde{T} + \mathcal{R}_{Su}} \right) \quad \text{with} \quad \mathcal{R}_{Su} = \frac{110.6K}{T^*_\infty} \tag{3.33}$$

Finally, the non-dimensional equation of state determines the resolved pressure

$$\overline{p} = \frac{\overline{\rho}\widetilde{T}}{\gamma Ma^2} . \tag{3.34}$$

For the current work, $\gamma = 1.4$ and $Pr = 0.70$.

The above equations contain three terms that do not occur in the unfiltered equations: the subgrid stress-tensor σ_{ik}, the subgrid heat-flux vector Q_k and the source term Π in the energy equation. These terms have to modelled (see section 3.4). In case of a DNS, where one assumes that all relevant time and length scales are resolved by the computational grid, the model terms are set to zero implying $\phi = \overline{\phi} = \widetilde{\phi}$. In the other limit, where the filter-width is so large that all fluctuations are filtered out, a traditional RANS is recovered.

3.4   Turbulence Models

If the numerical simulations are not performed in the DNS limit, a closure is needed for equations (3.27) - (3.29).

The subgrid heat-flux vector is modelled by assuming similarity in the gradient transport of heat and momentum, relating the thermal eddy diffusivity κ_T to the eddy diffusivity μ_T (see below) by a constant turbulent Prandtl number Pr_T as described in Speziale & So (1996)

$$Q_k = -\frac{1}{\gamma Ec}\frac{\mu_T}{Pr_T}\widetilde{T}_{,k} \, . \tag{3.35}$$

Speziale & So (1996) suggest that for most engineering applications a turbulent Prandtl number of $Pr_T = 0.9$ is adequate. Note that for a turbulent Prandtl number of unity complete similarity is assumed which is the well known Reynolds analogy for turbulent heat transfer.

The additional source term Π in the energy equation includes a pressure dilatation term, and terms involving turbulent dissipation and the subgrid mass-flux. It was shown by Sarkar *et al.* (1991) that not only the pressure dilatation term but also the compressible dissipation are important in compressible turbulence. Therefore, both effects are modelled according to Sarkar *et al.* (1991) and Sarkar (1992)

$$\overline{p'u''_{j,j}} = a_2 \bar{\rho}\sigma_{ik}\widetilde{S}_{ik}M_T + a_3\bar{\rho}\varepsilon M_T^2 \,, \tag{3.36}$$

with the turbulent Mach number (a measure of influence of compressibility on turbulence)

$$M_T = \sqrt{\frac{2K}{T}}M \quad , \quad M_T^* = \sqrt{\frac{2K^*}{a^*}} \,. \tag{3.37}$$

The turbulent dissipation is defined as $\overline{\tau''_{ik}u''_{i,k}} = \bar{\rho}\varepsilon$ and the subgrid mass-flux is modelled as $\overline{u''_i} = \dfrac{1}{\bar{\rho}\sigma_\rho}\mu_T\bar{\rho}_{,i}$. Combining these terms yields the extra source term :

$$\Pi = (1 - a_2 M_T)\,\bar{\rho}\sigma_{ik}\widetilde{S}_{ik} + \left(1 - a_3 M_T^2\right)\bar{\rho}\varepsilon - \left(\overline{\tau}_{ik} - \bar{p}\delta_{ik}\right)\left[\frac{\mu_T}{\sigma_\rho}\left(\frac{1}{\bar{\rho}}\right)_{,i}\right]_{,k} \,, \tag{3.38}$$

with the constants $a_2 = 0.15$ and $a_3 = 0.2$.

For the computation of the subgrid-stress-tensor σ_{ik}, an explicit algebraic stress model is used. It was derived from the explicit solution of the equilibrium form of the modelled Reynolds stress transport equation for incompressible flows in Gatski & Speziale (1993) and extended to compressible

flows by Speziale (1997). The model is of the form of an anisotropic eddy viscosity model with strain-dependent coefficients:

$$\sigma_{ik}^R = \frac{2}{3}K\delta_{ik} - \alpha_1^* \frac{K^2}{\varepsilon}\left(\widetilde{S}_{ik} - \frac{1}{3}\widetilde{S}_{jj}\delta_{ik}\right)$$
$$- \alpha_2^* \frac{K^3}{\varepsilon^2}\left(\widetilde{S}_{ij}\widetilde{W}_{jk} + \widetilde{S}_{kj}\widetilde{W}_{ji}\right)$$
$$+ \alpha_3^* \frac{K^3}{\varepsilon^2}\left(\widetilde{S}_{ij}\widetilde{S}_{jk} - \frac{1}{3}\widetilde{S}_{pq}\widetilde{S}_{pq}\delta_{ik}\right) . \tag{3.39}$$

To remove the possibility of singularities, a regularized version for α_i^* is used:

$$\alpha_i^* = \alpha_i \frac{3}{3 - 2\eta^2 + 6\xi^2} \approx \alpha_i \frac{3(1 + \eta^2)}{3 + \eta^2 + 6\eta^2\xi^2 + 6\xi^2} . \tag{3.40}$$

The terms η and ξ are related to the irrotational and the rotational strain rate invariants according to

$$\xi = \frac{\alpha_2}{\alpha_1}\frac{K}{\varepsilon}\left(\widetilde{W}_{pq}\widetilde{W}_{pq}\right)^{\frac{1}{2}} \tag{3.41}$$

$$\eta = \frac{1}{2}\frac{\alpha_3}{\alpha_1}\frac{K}{\varepsilon}\left(\widetilde{S}_{pq}\widetilde{S}_{pq}\right)^{\frac{1}{2}} . \tag{3.42}$$

For compressible calculations the constants α_i are given as $\alpha_1 = 0.37436$, $\alpha_2 = 0.11518$, and $\alpha_3 = 0.10799$. For "incompressible" boundary layer test-calculations the incompressible constants $\alpha_1 = 0.227$, $\alpha_2 = 0.0423$ and $\alpha_3 = 0.0396$ were used[1]. The turbulent eddy viscosity is given by

$$\mu_T = C_\mu \frac{\overline{\rho}K^2}{\varepsilon} \quad \text{with} \quad C_\mu = 0.09 \tag{3.43}$$

The turbulent kinetic energy K and the turbulent dissipation rate ε are computed solving two additional transport equations (see Wilcox (1998))

---

[1] For $\alpha_1 = 2C_\mu$ and $\alpha_2 = \alpha_3 = 0$ equation (3.39) reduces to the standard $K - \varepsilon$ model.

which are given here in dimensionless form:

$$\frac{\partial}{\partial t}\left(\bar{\rho}K\right) + \frac{\partial}{\partial x_k}\left[\bar{\rho}\widetilde{u}_k K - \left(\mu + \frac{\mu_T}{\sigma_K}\right)\frac{\partial K}{\partial x_k}\right] = -\Pi\,, \tag{3.44}$$

$$\frac{\partial}{\partial t}\left(\bar{\rho}\varepsilon\right) + \frac{\partial}{\partial x_k}\left[\bar{\rho}\widetilde{u}_k\varepsilon - \left(\mu + \frac{\mu_T}{\sigma_\varepsilon}\right)\frac{\partial\varepsilon}{\partial x_k}\right] = -C_{\varepsilon1}\bar{\rho}\frac{\varepsilon}{K}\sigma_{ik}\left(\tilde{u}_{i,k} - \frac{1}{3}\tilde{u}_{j,j}\delta_{ik}\right)$$

$$- C_{\varepsilon2}f_{\varepsilon2}\bar{\rho}\frac{\varepsilon^2}{K}$$

$$+ C_{\varepsilon3}\bar{\rho}Re_T^{\frac{1}{2}}\frac{\varepsilon^2}{K} - \frac{4}{3}\bar{\rho}\varepsilon\tilde{u}_{i,i}\,, \tag{3.45}$$

with the constants $\sigma_K = 1.0$, $\sigma_\varepsilon = 1.3$, $C_{\varepsilon1} = 1.44$, $C_{\varepsilon2} = 1.83$ and $C_{\varepsilon3} = 0.001$. The source term of eqn. 3.44 is the negative value of the source term in the energy equation because any production of turbulence kinetic energy must be equal to the dissipation of the averaged energy. The turbulent Reynolds number is defined as:

$$Re_T = \frac{\bar{\rho}K^2}{\bar{\mu}\varepsilon}\,. \tag{3.46}$$

To remove a singularity at walls (i.e., $K = 0$) in the destruction term of the ε-equation, a damping function of the form

$$f_{\varepsilon2} = 1 - exp\left(-Re\sqrt{0.1K}N\right) \tag{3.47}$$

is used, where N is the wall-normal distance. In the ASM model, this wall-damping function is the only term containing a wall distance, the Reynolds stress model automatically accounts for near wall effects through the computation of α_i^*. To be completely independent of any kind of wall function, the idea of Durbin (1993) is also implemented. It incorporates the assumption

that the smallest physical time-scale in a turbulent flow is the Kolmogorov time-scale. Therefore, by computing the turbulence time-scale as

$$\frac{K}{\varepsilon} = max\left[\frac{K}{\varepsilon}, C_T\sqrt{\frac{\overline{\mu}}{Re\overline{\rho}\varepsilon}}\right] \,, \tag{3.48}$$

with $C_T \approx 6$ and setting $f_{\varepsilon 2} = 1$, a completely wall-distance independent model is obtained.

3.5 Flow Simulation Methodology (FSM)

An important aspect of ongoing research is the application of the Flow Simulation Methodology (FSM). The fundamental concept of the methodology was already introduced in section 1. The details of the implementation are given now.

In FSM the turbulent stress tensor that is fed back to the filtered Navier-Stokes equation is scaled with a contribution function,

$$\sigma_{ij} = f(\Delta/L_k)\,\sigma_{ij}^R\,, \tag{3.49}$$

where $\Delta = [(\Delta x^2 + \Delta y^2 + \Delta z^2)/3]^{1/2}$ is the representative computational grid size and $L_k = \nu^{3/4}/\epsilon^{1/4}$ is the Kolmogorov length scale. The final form of $f(\Delta/L_k)$ has not yet been determined, but for the current work it was chosen to be of the form proposed by Speziale (1997):

$$f(\Delta/L_k) = \left(1 - e^{-\frac{\beta\Delta}{L_k}}\right)^n \,, \tag{3.50}$$

where β and n are adjustable parameters.

As the ratio $\frac{\beta\Delta}{L_k}$ becomes small (the grid resolution is sufficient to resolve structures the size of the Kolmogorov scale), $f(\Delta/L_k)$ approaches zero and the computation will approach the DNS-limit. For insufficient resolution, $f(\Delta/L_k)$ approaches unity and the RANS-limit is approached. For all intermediate values of the contribution function, a "non-traditional" Large Eddy Simulation (LES) based on a state-of-the-art Reynolds Stress model is performed.

4. NUMERICAL PROCEDURE

4.1 Overview

For the spatial derivatives, we are now using high order-accurate finite-difference approximations (sixth order in the axial and radial directions) and a pseudo-spectral (Fourier) decomposition in the azimuthal direction. This high accuracy is necessary for efficiently carrying out the highly demanding simulations of the dynamical behavior of the large structures in supersonic wake flows. In fact, during the years with funding from the ARO grant, we have drastically improved the spatial accuracy of our Navier-Stokes code. Direct Numerical Simulations of turbulent wake flows for higher Reynolds numbers, as performed in this research, require increasingly better numerical resolution for increasing Reynolds numbers as the size of the spatial scales decreases with Reynolds number. The use of finer and finer grids is limited by the memory and computing power of currently available supercomputers.

Therefore, using spatial difference approximations with higher accuracy will allow numerical resolution of the increasingly smaller scales without requiring a decrease of the grid intervals. From experience with our previous fourth-order-accurate code (using standard difference approximations) and from our experience using compact finite differences for incompressible simulations (Meitz & Fasel (2000)), we came to the conclusion that the consid-

erable demands regarding accuracy for simulations of turbulent supersonic wakes could be best met by employing compact difference approximations of at least fourth-order accuracy. Toward this end, we have entirely revamped our previously developed code and implemented compact differences where the order of accuracy is adjustable between fourth and sixth order. This is accomplished by allowing the coefficients in the approximations to be adjusted so that the accuracy (spectral accuracy) can be tailored to the particular needs of the simulation.

The advantage of employing high-order compact differences versus standard differences is apparent from Figure 4.1, where the numerically modified wave number of the computed scales is compared with the actual (physical) wave number of the scales (which should be resolved in the simulation). It is obvious that the drop-off in these modified wave numbers starts much earlier for a standard fourth-order approximation than for a compact difference of the same formal accuracy.

Use of methods with high accuracy, and thus employing compact differences, is equally beneficial for Large-Eddy Simulations (LES) and, in particular, for our new FSM (see discussion in 3.5). Of course, the higher accuracy allows use of larger step sizes for the Navier-Stokes computations for the resolved scales and therefore reduces demands on computer memory and computing power. In addition, and this is crucial, the higher accuracy allows
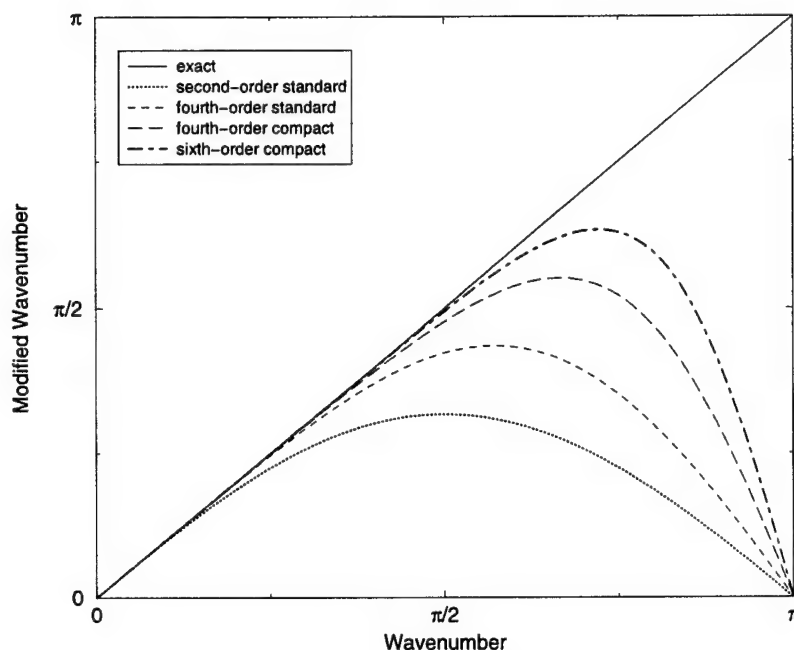
Figure 4.1 Modified wave number versus physical wave number. Comparison of standard and compact difference approximations.

rigorous testing and validation of the turbulence models (required for the unresolved subgrid scales), which have to be employed in LES. Using lower-order-accurate difference approximations does not allow a clean separation of the effects of the subgrid-scale turbulence model from the effects of the truncation error and, therefore, the role of the model cannot be scrutinized. In fact, in many LES investigations published in the literature, the truncation error of the numerical method played a more important role than the subgrid-scale model itself and therefore totally contaminated the results.

4.2 Vectorized Equations in Cylindrical Coordinates

All transport equations given in section 3 can be written in the form of an advection and a diffusion term on the left hand side and a source term on the right hand side. In cylindrical coordinates the structure is:

$$\frac{\partial U}{\partial t} + \frac{\partial A}{\partial z} + \frac{\partial B}{\partial r} + \frac{1}{r}\frac{\partial C}{\partial \theta} + \frac{1}{r}D = S. \tag{4.1}$$

with

$$U = \begin{pmatrix} U_1 \\ U_2 \\ U_3 \\ U_4 \\ U_5 \\ U_6 \\ U_7 \end{pmatrix} = \begin{pmatrix} \overline{\rho} \\ \overline{\rho}\widetilde{u} \\ \overline{\rho}\widetilde{v} \\ \overline{\rho}\widetilde{w} \\ \overline{\rho}E_R \\ \overline{\rho}K \\ \overline{\rho}\varepsilon \end{pmatrix} \tag{4.2}$$

$$A = \begin{pmatrix} A_1 \\ A_2 \\ A_3 \\ A_4 \\ A_5 \\ A_6 \\ A_7 \end{pmatrix} = \begin{pmatrix} \overline{\rho}\widetilde{u} \\ \rho\widetilde{u}^2 + \overline{p} - (\overline{\tau}_{zz} - \overline{\rho}\sigma_{zz}) \\ \rho\widetilde{u}\widetilde{v} - (\overline{\tau}_{rz} - \overline{\rho}\sigma_{rz}) \\ \rho\widetilde{u}\widetilde{w} - (\overline{\tau}_{\theta z} - \overline{\rho}\sigma_{\theta z}) \\ \rho\widetilde{u}H_R + \overline{q}_z + Q_z - \widetilde{u}\left(\overline{\tau}_{zz} - \overline{\rho}\sigma_{zz}\right) - \widetilde{v}\left(\overline{\tau}_{rz} - \overline{\rho}\sigma_{rz}\right) - \widetilde{w}\left(\overline{\tau}_{\theta z} - \overline{\rho}\sigma_{\theta z}\right) \\ \overline{\rho}\widetilde{u}K - \left(\frac{\mu}{Re} + \frac{\mu_T}{\sigma_K}\right)\frac{\partial K}{\partial z} \\ \overline{\rho}\widetilde{u}\varepsilon - \left(\frac{\mu}{Re} + \frac{\mu_T}{\sigma_K}\right)\frac{\partial \varepsilon}{\partial z} \end{pmatrix} \tag{4.3}$$

$$B = \begin{pmatrix} B_1 \\ B_2 \\ B_3 \\ B_4 \\ B_5 \\ B_6 \\ B_7 \end{pmatrix} = \begin{pmatrix} \overline{\rho}\widetilde{v} \\ \overline{\rho}\widetilde{u}\widetilde{v} - (\overline{\tau}_{rz} - \overline{\rho}\sigma_{rz}) \\ \overline{\rho}\widetilde{v}^2 + \overline{p} - (\overline{\tau}_{rr} - \overline{\rho}\sigma_{rr}) \\ \overline{\rho}\widetilde{v}\widetilde{w} - (\tau_{r\theta} - \overline{\rho}\sigma_{r\theta}) \\ \overline{\rho}\widetilde{v}H_R + \overline{q}_r + Q_r - \widetilde{u}\left(\overline{\tau}_{rz} - \overline{\rho}\sigma_{rz}\right) - \widetilde{v}\left(\overline{\tau}_{rr} - \overline{\rho}\sigma_{rr}\right) - \widetilde{w}\left(\overline{\tau}_{r\theta} - \overline{\rho}\sigma_{r\theta}\right) \\ \overline{\rho}\widetilde{v}K - \left(\frac{\mu}{Re} + \frac{\mu_T}{\sigma_K}\right)\frac{\partial K}{\partial r} \\ \overline{\rho}\widetilde{v}\varepsilon - \left(\frac{\mu}{Re} + \frac{\mu_T}{\sigma_K}\right)\frac{\partial \varepsilon}{\partial r} \end{pmatrix} \tag{4.4}$$

$$
C = \begin{pmatrix} C_1 \\ C_2 \\ C_3 \\ C_4 \\ C_5 \\ C_6 \\ C_7 \end{pmatrix} = \begin{pmatrix} \overline{\rho}\widetilde{w} \\ \overline{\rho}\widetilde{u}\widetilde{w} - \left(\overline{\tau}_{r\theta} - \overline{\rho}\sigma_{r\theta}\right) \\ \overline{\rho}\widetilde{v}\widetilde{w} - \left(\overline{\tau}_{r\theta} - \overline{\rho}\sigma_{r\theta}\right) \\ \overline{\rho}\widetilde{w}^2 + \overline{p} - \left(\overline{\tau}_{\theta\theta} - \overline{\rho}\sigma_{\theta\theta}\right) \\ \overline{\rho}\widetilde{w}H_R + \overline{q}_\theta + Q_\theta - \widetilde{u}\left(\overline{\tau}_{\theta z} - \overline{\rho}\sigma_{\theta z}\right) - \widetilde{v}\left(\overline{\tau}_{r\theta} - \overline{\rho}\sigma_{r\theta}\right) - \widetilde{w}\left(\overline{\tau}_{\theta\theta} - \overline{\rho}\sigma_{\theta\theta}\right) \\ \overline{\rho}\widetilde{w}K - \left(\frac{\mu}{Re} + \frac{\mu_T}{\sigma_K}\right)\frac{1}{r}\frac{\partial K}{\partial \theta} \\ \overline{\rho}\widetilde{w}\varepsilon - \left(\frac{\mu}{Re} + \frac{\mu_T}{\sigma_K}\right)\frac{1}{r}\frac{\partial \varepsilon}{\partial \theta} \end{pmatrix}
$$

$$(4.5)$$

$$
D = \begin{pmatrix} D_1 \\ D_2 \\ D_3 \\ D_4 \\ D_5 \\ D_6 \\ D_7 \end{pmatrix} = \begin{pmatrix} \overline{\rho}\widetilde{v} \\ \overline{\rho}\widetilde{u}\widetilde{v} - \left(\overline{\tau}_{rz} - \overline{\rho}\sigma_{rz}\right) \\ \overline{\rho}\widetilde{v}^2 - \overline{\rho}\widetilde{w}^2 - \left(\overline{\tau}_{rr} - \overline{\rho}\sigma_{rr}\right) + \left(\overline{\tau}_{\theta\theta} - \overline{\rho}\sigma_{\theta\theta}\right) \\ 2\overline{\rho}\widetilde{v}\widetilde{w} - 2\left(\overline{\tau}_{r\theta} - \overline{\rho}\sigma_{r\theta}\right) \\ \overline{\rho}\widetilde{v}H_R + \overline{q}_r + Q_r - \widetilde{u}\left(\overline{\tau}_{rz} - \overline{\rho}\sigma_{rz}\right) - \widetilde{v}\left(\overline{\tau}_{rr} - \overline{\rho}\sigma_{rr}\right) - \widetilde{w}\left(\overline{\tau}_{r\theta} - \overline{\rho}\sigma_{r\theta}\right) \\ \overline{\rho}\widetilde{v}K - \left(\frac{\mu}{Re} + \frac{\mu_T}{\sigma_K}\right)\frac{\partial K}{\partial r} \\ \overline{\rho}\widetilde{v}\varepsilon - \left(\frac{\mu}{Re} + \frac{\mu_T}{\sigma_K}\right)\frac{\partial \varepsilon}{\partial r} \end{pmatrix}
$$

$$(4.6)$$

$$
S = \begin{pmatrix} S_1 \\ S_2 \\ S_3 \\ S_4 \\ S_5 \\ S_6 \\ S_7 \end{pmatrix} = \begin{pmatrix} 0 \\ 0 \\ 0 \\ 0 \\ \Pi \\ \Pi_K \\ \Pi_\varepsilon \end{pmatrix}
$$

$$(4.7)$$

with Π, Π_K and Π_ε being the source terms given in equations 3.38, 3.44 and 3.45 respectively.

4.3   Azimuthal Fourier Transforms

Water tunnel results conducted by Siegel (1999) show that the flow picks a symmetry plane that moves on a time-scale much slower than that of interest for the unsteady structures in subsonic, incompressible flows. As in previous work on this topic by Tourbier (1996), symmetric Fourier transforms are therefore used in the azimuthal direction to achieve a significant reduction in

computing time. Previous work by Bourdon & Dutton (1998) shows that even the compressible flow shows some symmetry in azimuthal direction and the most recent publication by Bourdon & Dutton (2001) shows a clear symmetry of the flow in circumferential direction if delta-shaped disturbances on the body are used. Note that using symmetric transforms enforces a symmetry plane similar to the way the surface disturbances do in the experiment. For simplicity, only the equations for the DNS version of code (5 equations solved in vector form) are shown in Fourier space.

Replacing each flow variable with the appropriate sine- or cosine- transform gives

$$
\frac{\partial}{\partial t} \sum_{k=0}^{K} \begin{pmatrix} \hat{U}_1^k(r,z)\cos k\theta \\ \hat{U}_2^k(r,z)\cos k\theta \\ \hat{U}_3^k(r,z)\cos k\theta \\ \hat{U}_4^k(r,z)\sin k\theta \\ \hat{U}_5^k(r,z)\cos k\theta \end{pmatrix} + \frac{\partial}{\partial z} \sum_{k=0}^{K} \begin{pmatrix} \hat{A}_1^k(r,z)\cos k\theta \\ \hat{A}_2^k(r,z)\cos k\theta \\ \hat{A}_3^k(r,z)\cos k\theta \\ \hat{A}_4^k(r,z)\sin k\theta \\ \hat{A}_5^k(r,z)\cos k\theta \end{pmatrix} + \frac{\partial}{\partial r} \sum_{k=0}^{K} \begin{pmatrix} \hat{B}_1^k(r,z)\cos k\theta \\ \hat{B}_2^k(r,z)\cos k\theta \\ \hat{B}_3^k(r,z)\cos k\theta \\ \hat{B}_4^k(r,z)\sin k\theta \\ \hat{B}_5^k(r,z)\cos k\theta \end{pmatrix}
$$

$$
+ \frac{1}{r}\frac{\partial}{\partial \theta} \sum_{k=0}^{K} \begin{pmatrix} \hat{C}_1^k(r,z)\sin k\theta \\ \hat{C}_2^k(r,z)\sin k\theta \\ \hat{C}_3^k(r,z)\sin k\theta \\ \hat{C}_4^k(r,z)\cos k\theta \\ \hat{C}_5^k(r,z)\sin k\theta \end{pmatrix} + \frac{1}{r} \sum_{k=0}^{K} \begin{pmatrix} \hat{D}_1^k(r,z)\cos k\theta \\ \hat{D}_2^k(r,z)\cos k\theta \\ \hat{D}_3^k(r,z)\cos k\theta \\ \hat{D}_4^k(r,z)\sin k\theta \\ \hat{D}_5^k(r,z)\cos k\theta \end{pmatrix} = 0 \,. \tag{4.8}
$$

Commuting derivative and summation, and using the orthogonality of the sine and cosine function yields an equation for each Fourier mode k,

$$\frac{\partial}{\partial t} \begin{pmatrix} \hat{U}_1^k(r,z) \\ \hat{U}_2^k(r,z) \\ \hat{U}_3^k(r,z) \\ \hat{U}_4^k(r,z) \\ \hat{U}_5^k(r,z) \end{pmatrix} + \frac{\partial}{\partial z} \begin{pmatrix} \hat{A}_1^k(r,z) \\ \hat{A}_2^k(r,z) \\ \hat{A}_3^k(r,z) \\ \hat{A}_4^k(r,z) \\ \hat{A}_5^k(r,z) \end{pmatrix} + \frac{\partial}{\partial r} \begin{pmatrix} \hat{B}_1^k(r,z) \\ \hat{B}_2^k(r,z) \\ \hat{B}_3^k(r,z) \\ \hat{B}_4^k(r,z) \\ \hat{B}_5^k(r,z) \end{pmatrix} + \frac{1}{r} \begin{pmatrix} k\hat{C}_1^k(r,z) + \hat{D}_1^k(r,z) \\ k\hat{C}_2^k(r,z) + \hat{D}_2^k(r,z) \\ k\hat{C}_3^k(r,z) + \hat{D}_3^k(r,z) \\ -k\hat{C}_4^k(r,z) + \hat{D}_4^k(r,z) \\ k\hat{C}_5^k(r,z) + \hat{D}_5^k(r,z) \end{pmatrix} = 0,$$

(4.9)

$$k = 0, \ldots, K .$$

This set of equations is now solved with finite differences in the radial and streamwise direction as described in section 4.5.

4.4 Parity Conditions for Fourier Modes of Functions in Cylindrical Coordinates

Another challenge of this research has been the computation at the axis, which in cylindrical coordinates is represented by $r = 0$. The treatment of this boundary is discussed in the following. Axis boundary conditions are derived for the Fourier modes of functions in cylindrical coordinates that are necessary for the function to be smooth.

Consider smooth (C^∞) functions, either scalar, vector or second order tensor in a cartesian coordinates s, t rotated by angle ϕ. Smooth implies a convergent Fourier representation,

$$f(r,\theta) = \sum_{k=0}^{\infty} \hat{f}_k(r)e^{ik\theta} .$$

(4.10)

The complex representation is used only for convenience, as all functions of interest here are real-valued.

On s, the cylindrical coordinates and unit vectors are given by,

$$r = |s| \tag{4.11}$$

$$\theta = \begin{array}{l} \phi, \; s > 0 \\ \phi + \pi, \; s < 0 \end{array} \tag{4.12}$$

$$\frac{d^n}{ds^n} = \text{sgn}^n(s) \frac{d^n}{dr^n} \tag{4.13}$$

$$e^{ik\theta} = \text{sgn}^k(s) e^{ik\phi} \tag{4.14}$$

Parity conditions for the Fourier modes will be derived by requiring the existence of all derivatives on s at the origin. For the scalar case, this is

$$\lim_{s \to 0^-} \frac{d^n f}{ds^n} = \lim_{s \to 0^+} \frac{d^n f}{ds^n} \tag{4.15}$$

Even if f is a smooth function, radial derivatives of f need not be continuous at the origin due to the coordinate singularity. Even so, the Fourier modes of functions that are the radial derivatives of smooth functions have notable parity properties. These are seen almost by inspection of the Fourier representation, given that $\hat{f}_k(r)$ is either even or odd in r. One may note that any odd order of radial differentation will switch the parity "state" relative to the original function, while an even number will not.

Define "even parity" as being an even function in r in the even Fourier modes, while being an odd function in r in the odd modes. "Odd parity" is

then being an even function in the odd modes, etc. For functions with even parity,

$$\hat{f}_k^{(nr)}(r) = \begin{cases} \text{even} & k + n \text{ even} \\ \text{odd} & k + n \text{ odd} \end{cases} \qquad (4.16)$$

Functions with odd parity have

$$\hat{f}_k^{(nr)}(r) = \begin{cases} \text{even} & k + n \text{ odd} \\ \text{odd} & k + n \text{ even} \end{cases} \qquad (4.17)$$

Note that derivatives in θ do not change the parity of a function.

4.4.1 Scalars

The Fourier representation of f is

$$f(s) = \sum_{k=0}^{\infty} \hat{f}_k(|s|)e^{ik\phi}\text{sgn}^k(s) \,, \qquad (4.18)$$

or in general,

$$f^{(n)}(s) = \sum_{k=0}^{\infty} \hat{f}_k^{(n)}(|s|)e^{ik\phi}\text{sgn}^k(s)\text{sgn}^n(s) \,. \qquad (4.19)$$

Substituting this into equation 4.15,

$$\sum_{k=0}^{\infty} \hat{f}_k^{(n)}(0)e^{ik\phi}(-1)^{(k+n)} = \sum_{k=0}^{\infty} \hat{f}_k^{(n)}(0)e^{ik\phi} \qquad (4.20)$$

or

$$\sum_{k=0}^{\infty} \hat{f}_k^{(n)}(0)e^{ik\phi}\left[1 - (-1)^{(k+n)}\right] = 0 \qquad (4.21)$$

or

$$\sum_{k=0,n+k\,odd}^{\infty} 2\hat{f}_k^{(n)}(0)e^{ik\phi} = 0 \,. \qquad (4.22)$$

Since this is required for all ϕ,

$$\hat{f}_k^{(n)}(0) = 0, \forall\, n + k \text{ odd}, \tag{4.23}$$

that is, scalar functions have even parity.

4.4.2 Vectors

Consider now a smooth vector field $\mathbf{f}$ with (convergent) Fourier representation

$$\mathbf{f}(r, \theta, z) = \sum_{k=0}^{\infty} \left(\hat{f}_k(r, z)\mathbf{e}_r + \hat{g}_k(r, z)\mathbf{e}_\theta + \hat{h}_k(r, z)\mathbf{e}_z \right) e^{ik\theta} \tag{4.24}$$

with

$$\mathbf{e}_r = \text{sgn}(s)\mathbf{e}_s \tag{4.25}$$

$$\mathbf{e}_\theta = \text{sgn}(s)\mathbf{e}_t \tag{4.26}$$

On s, $\mathbf{f}$ is represented by,

$$\mathbf{f}(s, z) = \sum_{k=0}^{\infty} \left[\left(\hat{f}_k(|s|, z)\mathbf{e}_s + \hat{g}_k(|s|, z)\mathbf{e}_t \right) \text{sgn}(s) + \hat{h}_k(|s|, z)\mathbf{e}_z \right] e^{ik\phi} \text{sgn}^k(s) \tag{4.27}$$

Taking the n-th derivative in s and taking the two-sided limit as before, we obtain

$$0 = \sum_{k=0}^{\infty} \left\{ \begin{array}{l} \hat{f}_{k,nr}(0, z)\mathbf{e}_s \left[1 - (-1)^{n+k+1} \right] \\ +\hat{g}_{k,nr}(0, z)\mathbf{e}_t \left[1 - (-1)^{n+k+1} \right] \\ +\hat{h}_{k,nr}(0, z)\mathbf{e}_z \left[1 - (-1)^{n+k} \right] \end{array} \right\} e^{ik\phi} \tag{4.28}$$

or,

$$0 = \sum_{\substack{k=0 \\ n+k \text{ even}}}^{\infty} 2\hat{f}_{k,nr}(0,z)\mathbf{e}_s e^{ik\phi} \tag{4.29}$$

$$+ \sum_{\substack{k=0 \\ n+k \text{ even}}}^{\infty} 2\hat{g}_{k,nr}(0,z)\mathbf{e}_t e^{ik\phi}$$

$$+ \sum_{\substack{k=0 \\ n+k \text{ odd}}}^{\infty} 2\hat{h}_{k,nr}(0,z)\mathbf{e}_z e^{ik\phi}$$

Again invoking orthogonality,

$$\begin{aligned}
\hat{f}_{k,nr}(0,z) &= 0, \ n+k \text{ even} \\
\hat{g}_{k,nr}(0,z) &= 0, \ n+k \text{ even} \\
\hat{h}_{k,nr}(0,z) &= 0, \ n+k \text{ odd,}
\end{aligned} \tag{4.30}$$

so the radial and azimuthal vector components have odd parity, while the axial component has even parity.

4.5   Compact Differencing on Arbitrary Grids

The transport equations given in Fourier space in equation 4.3 are discretized with compact finite differences in the radial and streamwise direction. Sixth-order split compact finite difference stencils are derived in the following. These differences are valid on a non-equidistant grid instead of the usual mapping of the computational domain to a uniform grid. This results in greater flexibility of the choice of grids and was shown to lead to a lower truncation error by Meitz & Fasel (2000).

4.5.1 Derivation

Consider an ordered set of points $\{x_j\}$, with $x_i \neq x_j$ for $i \neq j$. It is helpful to define a characteristic grid spacing Δx which can be set as desired; $\Delta x = x_1 - x_0$ is chosen here. Note that this implies, mathematically at least, that the grid is refined uniformly. Define a dimensionless grid spacing by

$$\delta_k = \frac{x_k - x_0}{\Delta x} . \tag{4.31}$$

Define the finite difference stencil by

$$\sum_{k=k_1}^{k_2} a_k \left. \frac{\delta f}{\delta x} \right|_{x_k} = \frac{1}{\Delta x} \sum_{l=l_1}^{l_2} b_l f_l , \tag{4.32}$$

where it is assumed for simplicity that the stencil spans x_0 for both function values and derivatives, that is,

$$k_1 k_2 \leq 0 \tag{4.33}$$

$$l_1 l_2 \leq 0$$

The stencil is homogeneous in its coefficients. One condition on the coefficients can be selected arbitrarily.

$$\sum_{k=k_1}^{k_2} a_k = 1 \tag{4.34}$$

This is selected to allow a direct comparison of the truncation error term between compact and standard stencils. The expression for the truncation

error is

$$T = \left(\sum_{k=k_1}^{k_2} a_k \frac{\delta f}{\delta x}\Big|_{x_k} - \frac{1}{\Delta x}\sum_{l=l_1}^{l_2} b_l f_l\right) - \left(\sum_{k=k_1}^{k_2} a_k f'(x_k) - \frac{1}{\Delta x}\sum_{l=l_1}^{l_2} b_l f_l\right) \quad (4.35)$$

$$= \frac{1}{\Delta x}\sum_{l=l_1}^{l_2} b_l f_l - \sum_{k=k_1}^{k_2} a_k f'(x_k) \quad (4.36)$$

Expand $f'(x_k)$ in Taylor series about x_0. Since 0^0 is not defined, first pull

out the zero term in each sum.

$$T = \frac{1}{\Delta x}\sum_{l=l_1, l\neq 0}^{l_2} b_l f_l - \sum_{k=k_1, k\neq 0}^{k_2} a_k f'(x_k) + \frac{1}{\Delta x}b_0 f_0 - a_0 f_0' \quad (4.37)$$

$$= \frac{1}{\Delta x}\sum_{l=l_1, l\neq 0}^{l_2} b_l \sum_{j=0}^{\infty} f_0^{(j)}\frac{(x_l - x_0)^j}{j!} - \sum_{k=k_1, k\neq 0}^{k_2} a_k \sum_{j=0}^{\infty} f_0^{(j+1)}\frac{(x_k - x_0)^j}{j!} + \frac{1}{\Delta x}b_0 f_0 - a_0 f_0' \quad (4.38)$$

Exchange order of summation and shift an index

$$T = \frac{1}{\Delta x}b_0 f_0 - a_0 f_0' + \sum_{j=0}^{\infty} f_0^{(j)}\frac{1}{j!}\frac{1}{\Delta x}\sum_{l=l_1, l\neq 0}^{l_2} b_l(x_l - x_0)^j - \sum_{j=1}^{\infty} f_0^{(j)}\sum_{k=k_1, k\neq 0}^{k_2} a_k \frac{(x_k - x_0)^{j-1}}{(j-1)!} \quad (4.39)$$

Introduce dimensionless grid and collect like powers of Δx

$$T = \frac{1}{\Delta x}b_0 f_0 - a_0 f_0' + \sum_{j=0}^{\infty} \frac{f_0^{(j)}}{j!}\sum_{l=l_1, l\neq 0}^{l_2} b_l \delta_l^j \Delta x^{j-1} - \sum_{j=1}^{\infty} \frac{f_0^{(j)}}{j!}\sum_{k=k_1, k\neq 0}^{k_2} j a_k \delta_k^{j-1}\Delta x^{j-1} \quad (4.40)$$

$$T = \frac{1}{\Delta x}b_0 f_0 - a_0 f_0' + f_0 \sum_{l=l_1, l\neq 0}^{l_2} b_l \Delta x^{-1} + \sum_{j=1}^{\infty}\Delta x^{j-1}\frac{f_0^{(j)}}{j!}\left[\sum_{l=l_1, l\neq 0}^{l_2} b_l \delta_l^j - \sum_{\substack{k=k_1 \\ k\neq 0}}^{k_2} j a_k \delta_k^{j-1}\right] \quad (4.41)$$

$$T = \frac{1}{\Delta x}f_0 \sum_{l=l_1,}^{l_2} b_l - a_0 f_0' + \sum_{j=1}^{\infty}\Delta x^{j-1}\frac{f_0^{(j)}}{j!}\left[\sum_{l=l_1, l\neq 0}^{l_2} b_l \delta_l^j - \sum_{\substack{k=k_1 \\ k\neq 0}}^{k_2} j a_k \delta_k^{j-1}\right] \quad (4.42)$$

$$T = \frac{1}{\Delta x} f_0 \sum_{l=l_1,}^{l_2} b_l - a_0 f_0' + f_0' \left[\sum_{l=l_1, l \neq 0}^{l_2} b_l \delta_l - \sum_{k=k_1, k \neq 0}^{k_2} a_k \right] + \sum_{j=2}^{\infty} \Delta x^{j-1} \frac{f_0^{(j)}}{j!} \left[\sum_{l=l_1}^{l_2} b_l \delta_l^j - \sum_{k=k_1}^{k_2} j a_k \delta_k^{j-1} \right]$$

(4.43)

Note finally that $\delta_0 = 0$

$$T = \frac{1}{\Delta x} f_0 \sum_{l=l_1}^{l_2} b_l$$

(4.44)

$$+ f_0' \left[\sum_{l=l_1}^{l_2} b_l \delta_l - \sum_{k=k_1}^{k_2} a_k \right]$$

$$+ \sum_{j=2}^{\infty} \Delta x^{j-1} \frac{f_0^{(j)}}{j!} \left[\sum_{l=l_1}^{l_2} b_l \delta_l^j - \sum_{k=k_1}^{k_2} j a_k \delta_k^{j-1} \right]$$

A difference formula of order m requires all terms of order $n < m$ in Δx to be zero. Including the scaling equation, this gives,

$$\sum_{k=k_1}^{k_2} a_k = 1$$

(4.45)

$$\sum_{l=l_1}^{l_2} b_l = 0$$

(4.46)

$$\sum_{l=l_1}^{l_2} b_l \delta_l - \sum_{k=k_1}^{k_2} a_k = 0$$

(4.47)

$$\sum_{l=l_1}^{l_2} b_l \delta_l^j - \sum_{k=k_1}^{k_2} j a_k \delta_k^{j-1} = 0, j = 2, .., m$$

(4.48)

As expected, a stencil of order m requires $m+2$ equations. This is the same as the number of known values in the stencil, (function value and derivatives). When these conditions are met, the truncation error becomes,

$$T = \Delta x^m \frac{f_0^{(m+1)}}{(m+1)!} \left[\sum_{l=l_1}^{l_2} b_l \delta_l^{(m+1)} - \sum_{k=k_1}^{k_2} (m+1) a_k \delta_k^m \right]$$

(4.49)

This can be arranged in a matrix equation and solved for specific grid point values. Alternately, the matrix can be inverted symbolically using a computer algebra system such as Maple or Mathematica, and the solution translated directly into source code.

4.5.2 Analysis of the compact difference stencils

4.5.2.1 Modified Wavenumber

Examine the effect of equation 4.32 when applied to a single mode $f(x) = e^{i\kappa x}$. The exact derivative is

$$\frac{\partial}{\partial x}f = i\kappa e^{i\kappa x} \tag{4.50}$$

where κ will be called the exact wavenumber. Define the modified wavenumber κ' by

$$\frac{\delta f}{\delta x} = i\kappa' e^{i\kappa x}, \tag{4.51}$$

κ' is found by substituting 4.51 into 4.32.

$$\kappa'\Delta x = -i\frac{\sum_{l=l_1}^{l_2} b_l e^{i\kappa\Delta x\delta_l}}{\sum_{k=k_1}^{k_2} a_k e^{i\kappa\Delta x\delta_k}} \tag{4.52}$$

4.5.2.2 Amplitude and Phase Error

Consider the linear model convection equation in one dimension,

$$\frac{\partial}{\partial t}f - c\frac{\partial}{\partial x}f = 0 \tag{4.53}$$

with initial condition

$$f(x,0) = e^{i\kappa x} \tag{4.54}$$

The exact solution at $t = \Delta t$ is

$$f(x, \Delta t) = e^{i\kappa(x - c\Delta t)} \tag{4.55}$$

$$= e^{i\kappa x} e^{-i\nu(\kappa \Delta x)} \tag{4.56}$$

where ν is the CFL number. We characterize this by the exact amplitude and phase, given by

$$A = |e^{-i\nu(\kappa \Delta x)}| = 1 \tag{4.57}$$

$$\Phi = -\nu\kappa\Delta x \tag{4.58}$$

If the standard fourth order Runge-Kutta scheme is applied to equation 4.53 along with an approximate x-derivative,

$$f(x, \Delta t) = e^{i\kappa x} \sum_{k=0}^{4} \frac{1}{k!} \left(-i\nu\kappa'\Delta x\right)^k . \tag{4.59}$$

The numerically obtained amplitude and phase are then

$$A' = |\sum_{k=0}^{4} \frac{1}{k!} \left(-i\nu\kappa'\Delta x\right)^k | \tag{4.60}$$

$$\Phi' = \arg \left[\sum_{k=0}^{4} \frac{1}{k!} \left(-i\nu\kappa'\Delta x\right)^k \right] \tag{4.61}$$
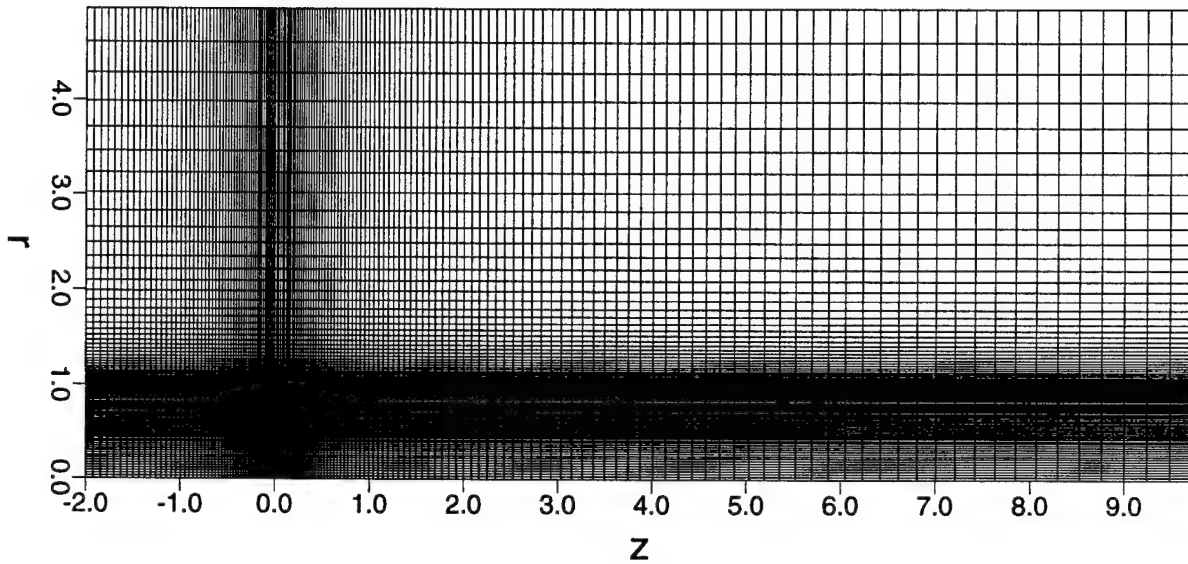
Figure 4.2 Radially and axially stretched grid for typical DNS (full domain extends to $r = 10$ and $z = 25$, only every other grid point shown).

Examples are shown for an exponentially stretched grid and various compact stencils in figures 4.3 and 4.4. A typical grid for a DNS is shown in figure 4.2.

Figures 4.3 and 4.4 show an analysis of different spatial discretizations in combination with a fourth-order Runge-Kutta method at $CFL = 0.15$ applied to the linear wave equation. It becomes clear that the sixth-order compact differences have a far superior wave-number accuracy (see Modified Wavenumber plot). However, when the stretching of the grid is accounted for in the analysis, the amplitude plot shows that for stretching factors larger than unity, amplification will occur in the higher wave-number region. Therfore, a spatial filter has to be employed. For this research, a fourth-order compact filter was chosen.
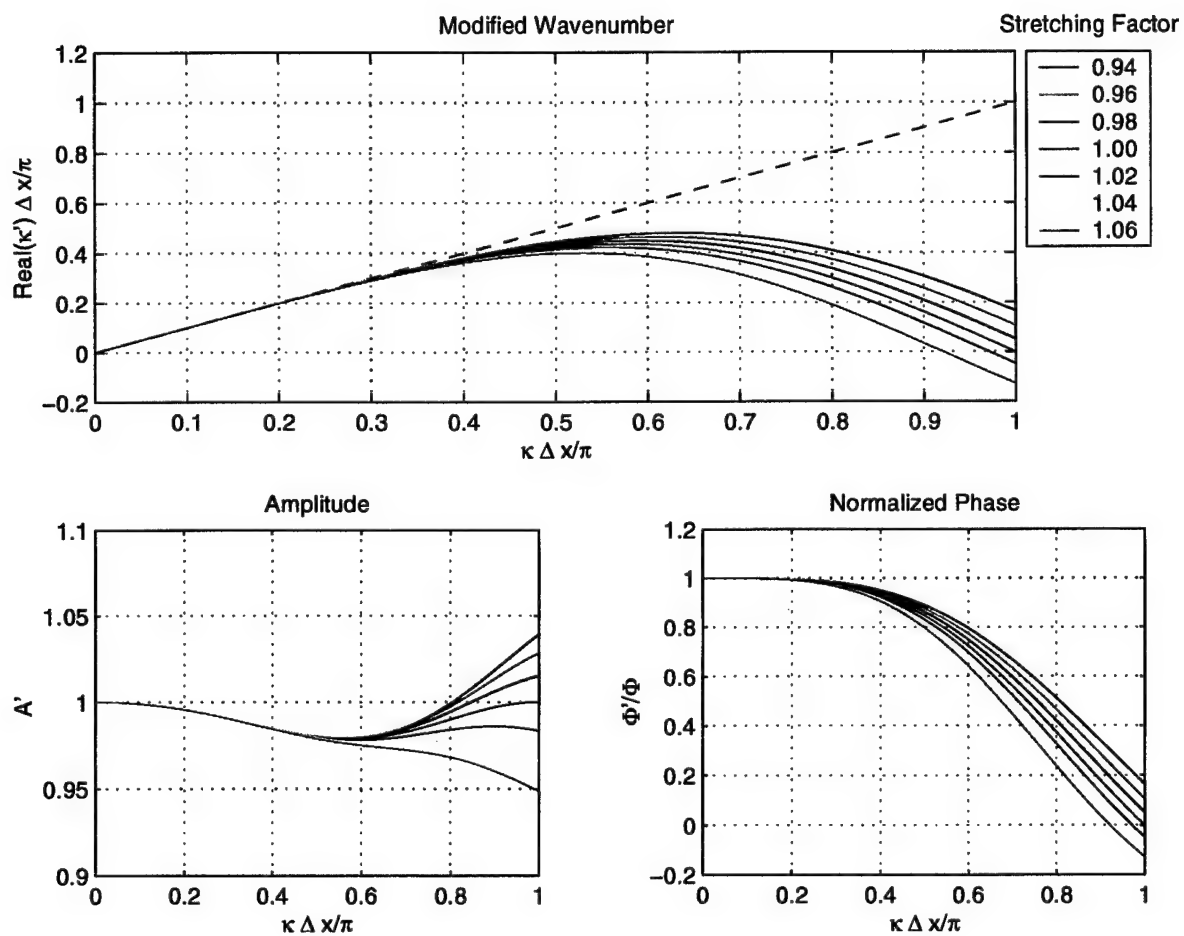
Figure 4.3 Modified wavenumber, Amplitude and Phase distribution for a fourth order explicit scheme on a stretched grid in combination with a fourth-order Runke-Kutta time-integration for $CFL = 0.15$
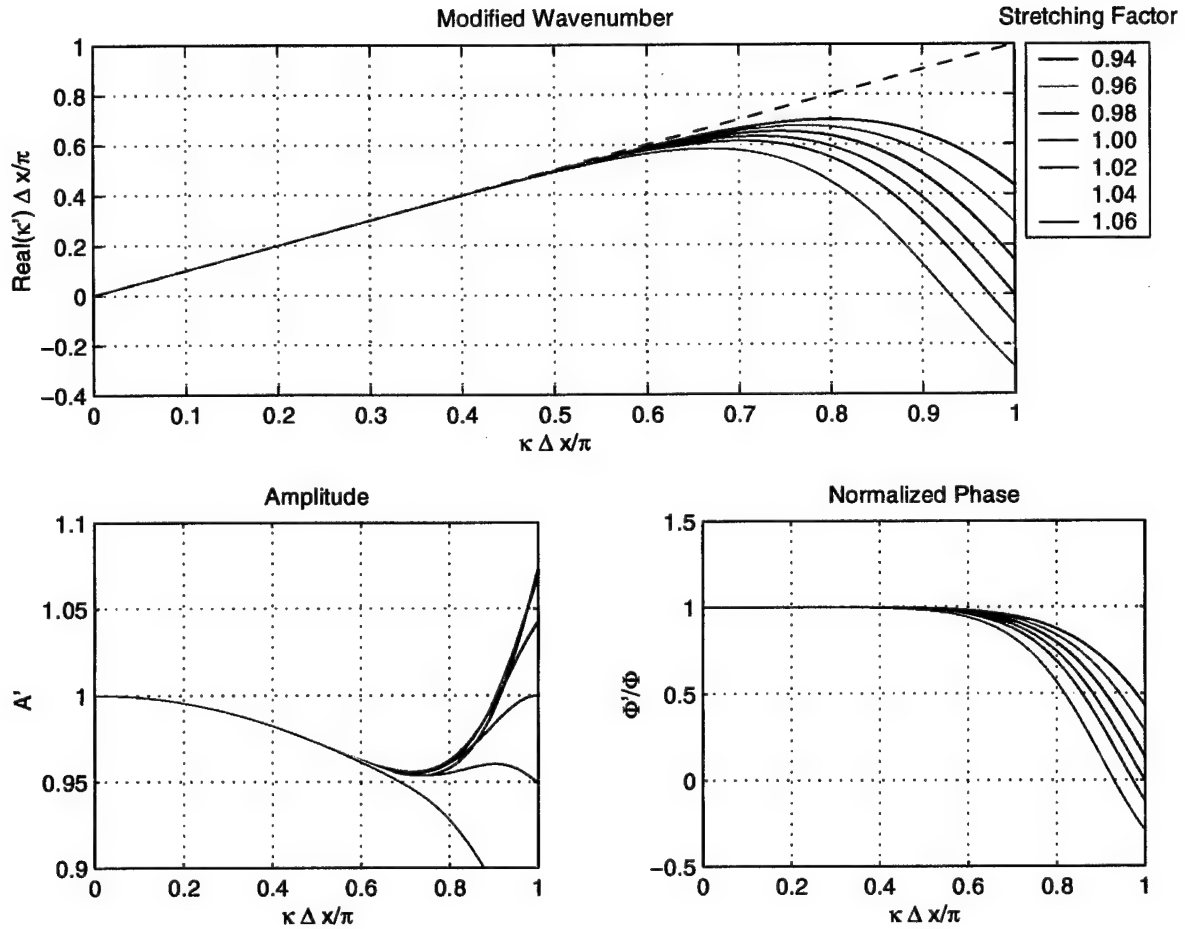
Figure 4.4 Modified wavenumber, Amplitude and Phase distribution for a sixth order compact scheme on a stretched grid in combination with a fourth-order Runke-Kutta time-integration for $CFL = 0.15$

4.6   Time Integration

A fourth-order Runge-Kutta method is used for the time-discretization. In this case, four intermediate timesteps are used, which Ferziger (1981) writes as

$$\phi_1 = \phi_n + \frac{\Delta t}{2} f(\phi_n)$$

$$\phi_2 = \phi_n + \frac{\Delta t}{2} f(\phi_1) \tag{4.62}$$

$$\phi_3 = \phi_n + \Delta t f(\phi_2)$$

$$\phi_{n+1} = \phi_n + \frac{\Delta t}{6} \left[f(\phi_n) + 2f(\phi_1) + 2f(\phi_2) + f(\phi_3)\right] .$$

If the first three steps are substituted into the last, the result is

$$\phi_{n+1} = \phi_n + \Delta t f(\phi_n) + \frac{\Delta^2 t}{2} f^2(\phi_n) + \frac{\Delta^3 t}{6} f^3(\phi_n) + \frac{\Delta^4 t}{24} f^4(\phi_n) . \tag{4.63}$$

Thus, the method is of fourth order in Δt. As written above, three intermediate levels of variables (ϕ_1, ϕ_2, ϕ_3) are needed. With some manipulation, the form used in the code can be obtained, which uses only two intermediate

variables:

$$\phi_1 = \phi_n + \frac{\Delta t}{2} f(\phi_n)$$

$$\phi_2 = \phi_n + \frac{\Delta t}{2} f(\phi_1)$$

$$\phi_1 = \phi_1 + 2\phi_2 \tag{4.64}$$

$$\phi_2 = \phi_n + \Delta t f(\phi_2)$$

$$\phi_1 = \frac{1}{3} \left(-\phi_n + \phi_1 + \phi_2 \right)$$

$$\phi_{n+1} = \phi_1 + \frac{\Delta t}{6} f(\phi_2) \,.$$

4.7 Integration Domain

For the numerical simulations, the integration domain is divided into two sub-domains. One domain contains the boundary layer on the axisymmetric body and extends to the corner of the base. The second domain starts at the base and extends to the outflow boundary (Figure 4.5). As in the simulations by Tourbier (1996) only the last part of the approach flow is computed with the inflow boundary layer being another parameter in the simulation.

The numerical simulations are performed in two steps. In the first step, a steady base flow is computed by solving the Navier Stokes equation for an axisymmetric geometry. In the second step, the unsteady, three dimensional flow is computed using the steady base flow (computed in step 1) as the initial condition. Thus, the Navier-Stokes code consists of two main components,
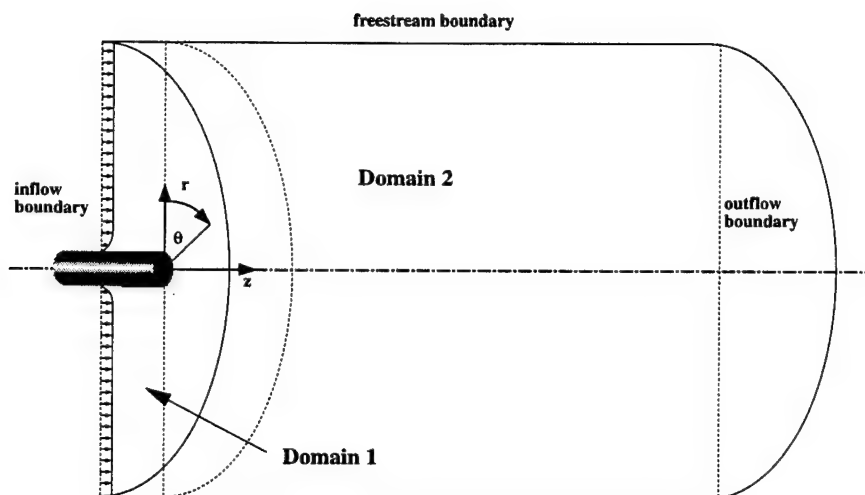
Figure 4.5 Computational Domain.

one for calculating the steady, axisymmetric base flow and the other for calculating the unsteady three dimensional flow.

4.8 Boundary Conditions

For the inflow boundary, the axial and azimuthal velocity and the temperature are set to a constant value. In a subsonic calculation, either a Dirichlet condition for pressure and turbulent kinetic energy and dissipation rate and a Neumann condition on radial velocity can be set or vice versa. For supersonic simulations the pressure is fixed in the supersonic region and a Neumann condition is used in the subsonic part of the boundary layer.

The outflow boundary is computed via one-sided stencils, setting the

second derivative to zero. Only for subsonic cases, the pressure can be set to a constant value.

The freestream boundary is set according to Thompson (1987) for supersonic cases. In subsonic cases, this siplifies to Neumann conditions.

At the walls, no slip and no penetration is enforced on all velocity components and the turbulent kinetic energy is set to zero. Pressure can be either computed at the wall through the wall-normal momentum equation or a Neumann condition can be applied. Temperature can be set to a constant value or computed through a high-order extrapolation, i.e. either isothermal or adiabatic walls are specified.

For all boundaries mentioned above, the density is computed through the equation of state for a perfect gas.

5.   CODE VALIDATION

5.1   Navier-Stokes Code for DNS

For validation of the first component of the Navier-Stokes code (for calculating the steady axisymmetric base flow), an axisymmetric wake for a free stream Mach number of $M = 0.2$ and a global Reynolds number of $Re_D = 1,000$ was calculated and compared to results from a calculation using an incompressible Navier-Stokes code developed by Schwarz *et al.* (1994) $[Re_D = (u_\infty D)/\nu_\infty$, where D is the diameter of the body]. For the incompressible simulations, the Navier-Stokes code of Schwarz *et al.* (1994) is based on a vector potential vorticity formulation. In addition, the numerical components of the code are also very different from the ones used in our present code. Comparisons between the compressible and incompressible simulations have shown very good agreement. Comparison of a global quantity, the length of the recirculation zone, and a local quantity of the flow field, the azimuthal vorticity at the corner of the base, showed practically identical results. For validation of the other component of the Navier-Stokes code for calculating the unsteady (disturbed) flow, the response of the steady subsonic flow field for $M = 0.2$ and $Re_D = 1,000$ (obtained from the steady calculation as discussed above) to a three dimensional disturbance input was calculated and compared to calculations by Schwarz *et al.* (1994). The dis-

turbance was generated by a single pulse at one location in the near wake region. With this disturbance generation, a broad spectrum of disturbance frequencies is introduced into the flow field. From the incompressible simulations by Schwarz *et al.* (1994), it was found that, for the global Reynolds number of $Re = 1,000$, the flow field includes a region of absolute instability with regard to three dimensional (helical) disturbances. For additional validation of the DNS code, we calculated the response of the flow for the same conditions as above ($M = 0.2$, $Re_D = 1,000$) to strong, nonlinear, continuous excitations through a blowing and suction slot. The disturbances introduced were purely in the first helical Fourier mode (k=1). The results were directly compared to experiments that were conducted in our hydrodynamics laboratory water channel. A typical response of the flow field is shown in Figure 5.1, where instantaneous contour lines of constant azimuthal vorticity are shown. In this view, the flow field exhibits energetic alternating structures (with an amplitude of 15% of the free stream velocity) that are strongly periodic. In fact, Figure 5.2, which is for the same time instant, a view of a plane 90° from that in Figure 5.1, confirms that this instantaneous flow field consists of two counter-rotating helical modes. Numerical flow visualization obtained from the DNS data, as shown in Figure 5.3 and 5.4, was also compared to physical flow visualization of the laboratory experiments. The agreement between numerical and experimental observations was remarkable. As in the
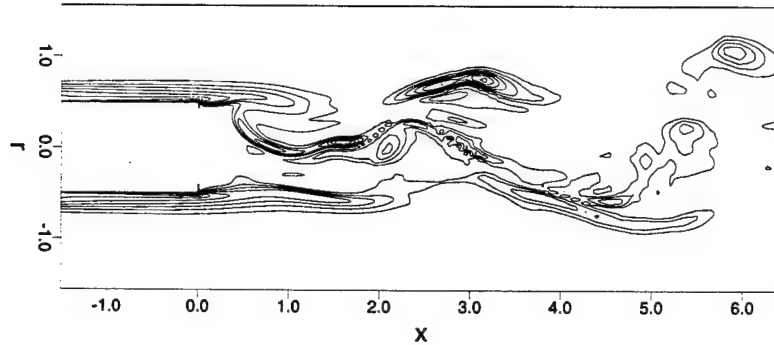
Figure 5.1 Isocontours of constant azimuthal vorticity for $M = 0.2$ and $Re = 1,000$, $\theta = 0°$.

experiments, the frequency of the developing structures also locked in to that of the forcing frequency.

5.2 Reynolds Averaged Navier Stokes

The turbulence model was first validated with a flat plate, zero pressure gradient turbulent boundary layer because of the available data for this case and the experience our research group has had with that case in the past. Figure 5.5 shows the streamwise velocity in wall coordinates to emphasize the near-wall behavior. The simulations were run using the ASM in domain 1 (see figure 4.5) at $M = 0.2$ with the incompressible coefficients α_i given in section 3.4. As initial condition, a laminar boundary layer profile was cho-
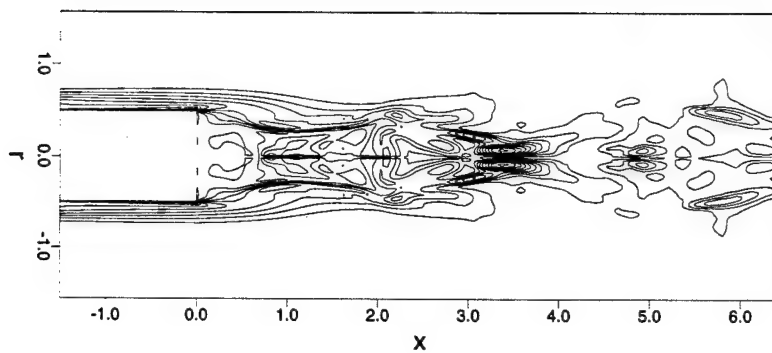
Figure 5.2 Isocontours of constant azimuthal vorticity for $M = 0.2$ and $Re = 1,000$, $\theta = 90°$

Figure 5.3 Flow visualization using particles. From DNS data: $M = 0.2$ and $Re = 1,000$, $\theta = 0°$.

Figure 5.4 Flow visualization using particles. From DNS data: $M = 0.2$ and $Re = 1,000$, $\theta = 90°$
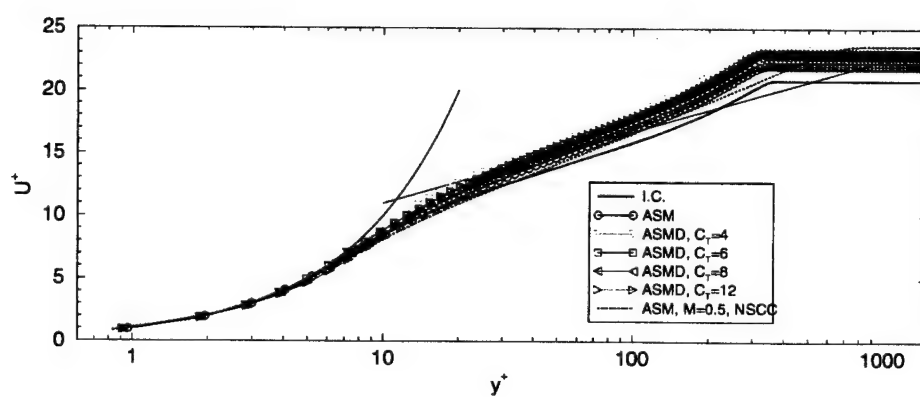
Figure 5.5 Streamwise velocity in wall-coordinates for turbulent boundary layer (incompressible model).

sen for the velocity field and both turbulent quantities K and ε were set to a constant (typically 10^{-3}) throughout the domain. A derivative condition was prescribed for K and ε at the inflow. This method was chosen to ensure that the numerical procedure is capable not only of maintaining a correct solution but also of producing a meaningful result from conditions that differ significantly from the desired final state. The results of an ASM case using the ramping function $f_{\varepsilon 2}$ and computations of the wall distance independent ASM (see equation 3.48), varying the constant C_T, are compared to the theoretical curves (laminar sublayer with $U^+ = y^+$ and logarithmic law region with $U^+ = 2.5 log(y^+) + 5.1$) and a case run by D. von Terzi using a compressible code in Cartesian coordinates written in C (NSCC). All simulations share a slope that is slightly too steep, but otherwise the agreement to the theoretical curves is satisfactory.

5.3 ASM Results for Subsonic Wakes

Initially, the turbulence model was tested in "full wake mode" for an incompressible case at $M = 0.2$ with $Re_D = 100,000$ to demonstrate the ability of the ASM to capture unsteady structures (the incompressible case develops larger structures due to the lack of the damping due to compressibility). A typical result is shown in figure 5.6. Shown are instantaneous contours of vorticity and it is clearly visible that the shear layer develops a strong insta-
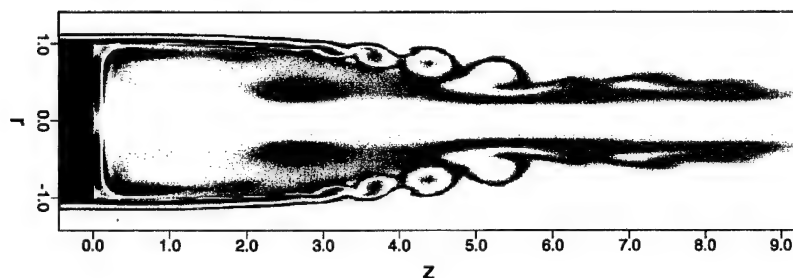
Figure 5.6 Instantaneous contours of azimuthal vorticity for 2D-URANS; $Re_D = 100,000$; $M = 0.2$.
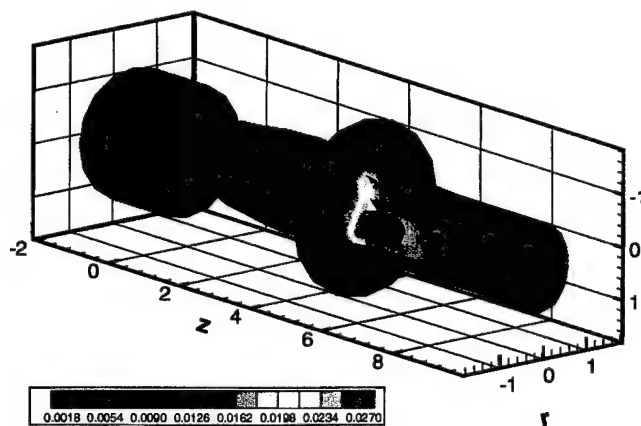
Figure 5.7 3-dimensional distribution of turbulent kinetic energy for 3D-URANS; $Re_D = 100,000$; $M = 0.2$.

bility with roll-up of vortices even if the turbulence model is fully switched on and no external forcing is applied.

Several 3-D URANS computations were carried out for the same subsonic test case. Figure 5.7 clearly shows that the distribution of turbulent kinetic energy has significant variation in azimuthal direction and, therefore, justifies the approach of coding all turbulent variables fully three-dimensional.

5.4 Flow Simulation Methodology

In addition, we have implemented the new Flow Simulation Methodology (FSM) together with the new turbulence models that are an integral part of FSM. We have tested and validated almost all of the critical individual modules of the FSM.

Typical results from validating the individual modules of FSM are presented in Figures 5.8 and 5.9. These figures were selected to demonstrate the role of the contribution function $f(\Delta/L_K)$, (equation 3.50), which is the crucial element of the FSM. An incompressible turbulent flat-plate boundary layer was chosen for this validation because a wealth of experimental, theoretical, and numerical data is available for comparison. Shown in Figures 5.8 and 5.9 are color contours of instantaneous spanwise vorticity and overlaid are isolines of instantaneous kinetic energy. The results in Figures 5.8 and 5.9 are from FSM calculations with different values of β (equation 3.50). A large value of β leads to a larger contribution of the turbulence model to the stresses, which in essence is equivalent to carrying out a simulation with a coarser grid [for Figure 5.9]. Therefore, comparing Figures 5.8 and 5.9, it is obvious that details of the flow due to smaller structures are removed when the contribution of the model is increased. Nevertheless, the high coherence of vorticity and turbulent kinetic energy is remarkable, even as fewer details
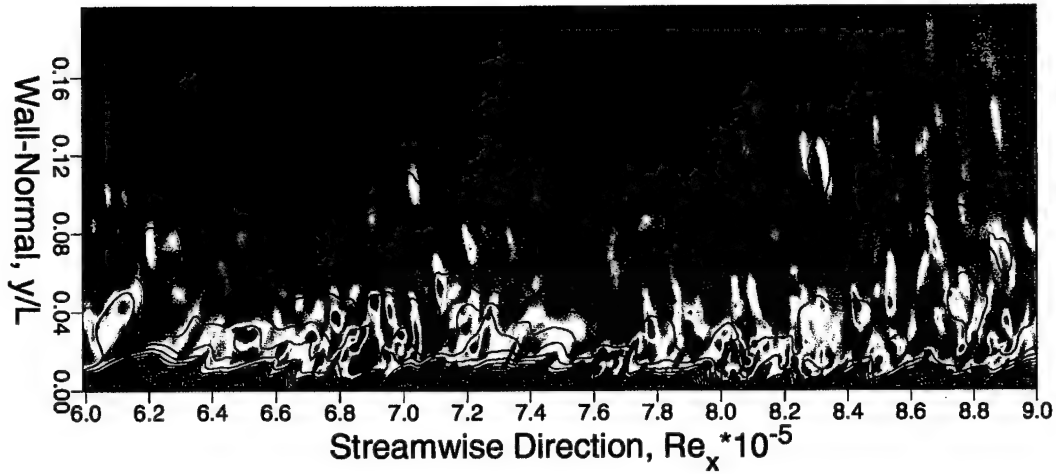
Figure 5.8 FSM applied to turbulent flat-plate boundary layer (incompressible). Color contours of instantaneous spanwise vorticity and isolines of instantaneous turbulent kinetic energy: FSM: $\beta = 0.02$.

of the instantaneous flow field are resolved.

As discussed in section 3.5, with $f(\Delta/L_K)$, the contribution of the turbulence model adjusts locally and instantaneously during the simulation from which Figures 5.8 and 5.9 were obtained. For example, for the same boundary layer simulation, Figure 5.10 shows the time-averaged $f(\Delta/L_K)$. It is obvious that the contribution function behaves as expected. The contribution of the model is large close to the wall, where the physical resolution (grid size compared to Kolmogorov length scale) is coarse. The contribution then decreases since the Kolmogorov scale increases with increasing distance from the wall. This is a clear demonstration that the contribution function, equation 5.10, is performing as it was designed to perform.

Figure 5.9 FSM applied to turbulent flat-plate boundary layer (incompressible). Color contours of instantaneous spanwise vorticity and isolines of instantaneous turbulent kinetic energy: FSM: $\beta = 0.05$.
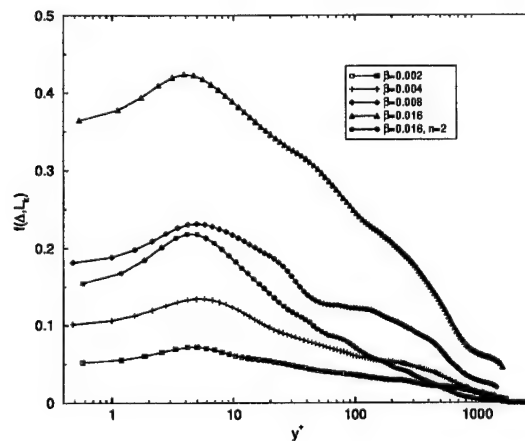
Figure 5.10 Time-averaged profiles of $f(\Delta/L_K)$ relative to local boundary layer thickness for cases shown in Figures 5.8 and 5.9 and for larger values of $f(\Delta/L_K)$.

6. RESULTS

6.1 DNS

6.1.1 Steady (Undisturbed Flow)

We have performed supersonic calculations for a Mach number of $M = 2.46$ [experiments of Herrin & Dutton (1991) and the Reynolds averaged calculations by Sahu (1992)]. We made calculations for different Reynolds numbers in order to explore the effect of Reynolds number on the resulting flow field. For the same Reynolds number as for the subsonic case, $Re_D = 1,000$, the base pressure was found to be much lower for the supersonic case than for the subsonic case, which is consistent with the experimental observations of Herrin & Dutton (1991). However, in the experiments, the pressure distribution was found to be practically constant along the base, while it varied by almost 20% in the numerical results. A variation of pressure along the base was also found in the Reynolds averaged calculations (using turbulence models) by Sahu (1992) and by Sturek & Nietubicz (1992). One may speculate that the different behavior of the base pressure along the base is due to the action of the large structures, which is not included in our steady base flow calculations and may not be adequately represented in the turbulence models used in the Reynolds averaged calculations. In fact, results from our numerical simulations discussed below support this conjecture. An
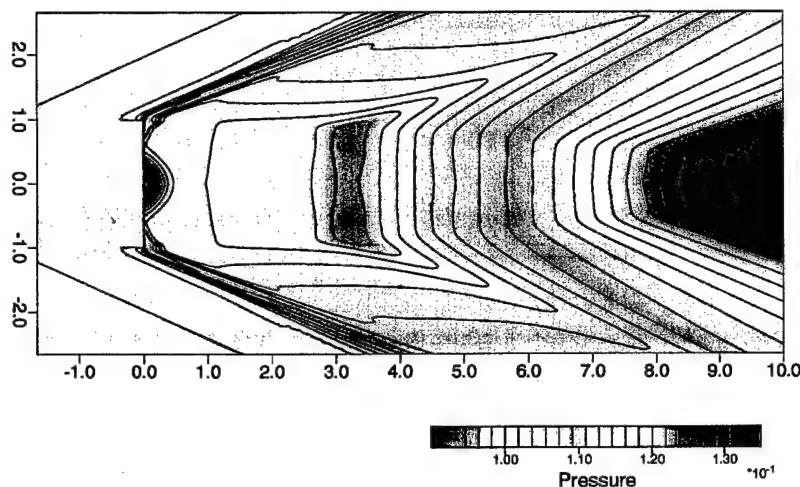
Figure 6.1 Contours of constant pressure for $Re = 18,000$, $M = 2.46$.

answer to this speculation is of considerable relevance for the development

of improved turbulence models. In order to obtain a closer comparison with

the experimental data by Herrin & Dutton (1991), we also calculated steady

flow fields for Reynolds numbers up to $Re_D = 100,000$, with a boundary

layer thickness at the corner of $\delta = 0.07D$, which matched the boundary

layer thickness of the experiment. A typical result for $Re_D = 18,000$ in the

form of constant pressure contours is shown in Figure 6.1.

6.1.2 Unsteady (Disturbed) Three-Dimensional Flow.

To investigate the absolute stability behavior of the supersonic base flow,

a pulse disturbance was introduced into the recirculation region. For the first

calculation, we used the same Reynolds number as for the incompressible cal-

culation ($Re_D = 1,000$). After an initially very short strong response of the

flow field, the disturbances decayed everywhere. Increasing the Reynolds

number, $2,000 \leq Re_D \leq 25,000$, showed no difference in the disturbance response: disturbances decayed after a relatively short time with the exception that the decay rate decreased with increasing Reynolds number. Thus, in contrast to the subsonic case, where an absolute instability exists with respect to helical disturbance modes, the calculations for $M_\infty = 2.46$ and Reynolds numbers up to $Re_D = 25,000$ showed no indication of absolute instability with respect to helical or axisymmetric modes. Therefore, it appears, as has been expected, that supersonic wake flows are more stable than their incompressible counterparts. This conjecture is consistent with the findings of Chen *et al.* (1990) for a two dimensional compressible wake, where the growth rates of disturbances were found to be up to an order of magnitude smaller than for a comparable incompressible wake and structures appeared to diffuse much faster.

6.1.3 Search for Absolute Instability for Supersonic Axisymmetric Base Flows

As seen from the previous discussion, the results for the supersonic flow field of $M = 2.46$ and Reynolds numbers up to $Re_D = 25,000$ do not exhibit an absolute instability. Since compressibility has a stabilizing effect (as discussed above), we decided to perform a simulation for a lower Mach number to see if an absolute instability would arise. Thus, we calculated the flow field for a Mach number of $M = 1.2$ and $Re_D = 4,000$ (Tourbier & Fasel
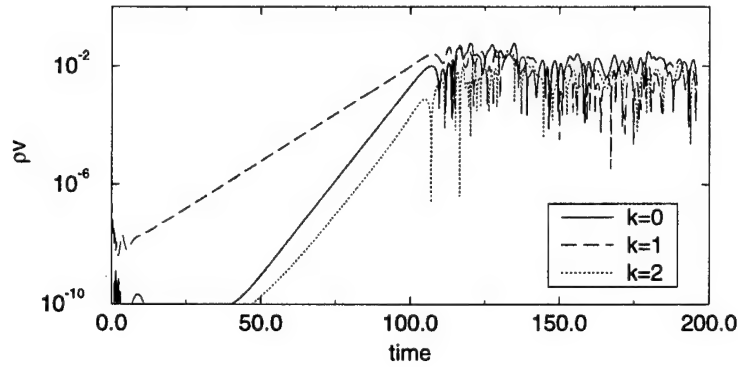
Figure 6.2 Time response of radial momentum at $z = 0.5$ and $r = 0.5$ for three different azimuthal Fourier modes (k) to a three-dimensional pulse disturbance in the near wake for $M = 1.2$ and $Re_D = 4,000$.

(1994)). As before, the flow field was disturbed by introducing a single pulse locally in the recirculation region. A typical temporal response of the flow field is given in Figure 6.2. It is obvious that, for different azimuthal Fourier modes, the disturbance grows exponentially in time until it reaches a state of nonlinear saturation. This is a clear manifestation of the existence of an absolute instability.

An impression of the instantaneous flow field can be obtained from Figures 6.3 and 6.4. Shown are instantaneous contour lines of the azimuthal vorticity after the disturbance has reached the state of nonlinear saturation. Large structures can be observed in the near-wake region. In order to investigate the influence of the structures on the global flow field, the (time-averaged)
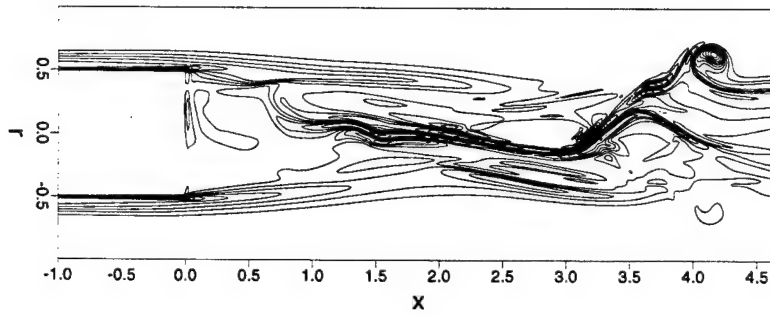
Figure 6.3 Isocontours of constant azimuthal vorticity for $M = 1.2$ and $Re = 4,000$, $\theta = 0°$.
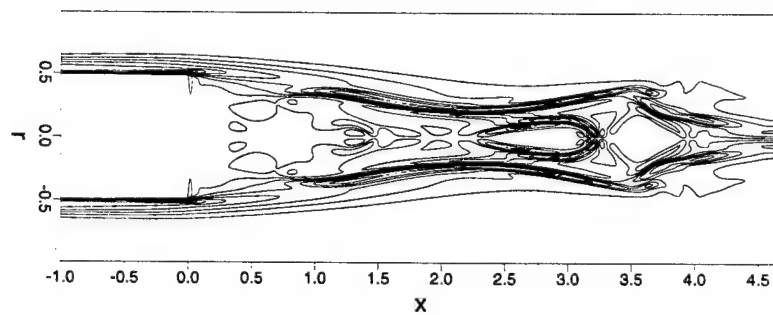
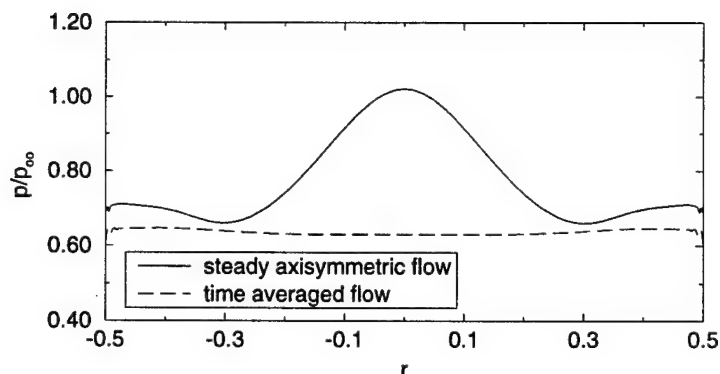Figure 6.4 Isocontours of constant azimuthal vorticity for $M = 1.2$ and $Re = 4,000$, $\theta = 90°$
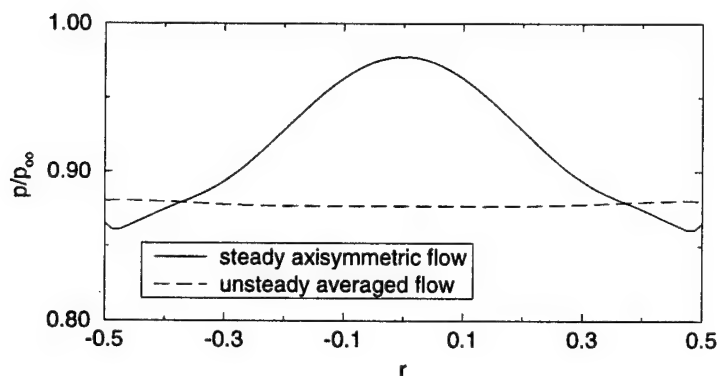
Figure 6.5 Base pressure distribution for a steady axisymmetric flow field and a time-averaged unsteady flow field for $M = 1.2$ and $Re = 4,000$.

mean flow was calculated. A comparison of the base pressure obtained from a steady calculation and that obtained from a time-averaged mean flow calculation is shown in Figure 6.5. Clearly, the presence of the large structures causes a drop in the base pressure. Also, for the unsteady calculation, the distribution of the pressure along the base is virtually constant, which agrees with observations in experiments, while pressure varies strongly for the steady calculation. These results are a strong indication that the action of the large structures is responsible for the flat base pressure distribution observed in experiments. Thus, there is further evidence that this may also be the reason why Reynolds-averaged calculations have difficulties in reproducing the flat pressure distribution.

In other simulations for $M = 2.46$, we pushed the Reynolds number to $Re_D = 100,000$. As before, the flow field was disturbed by a single
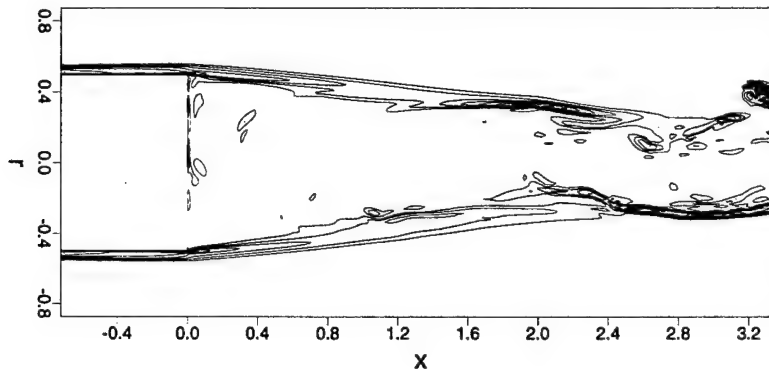
Figure 6.6 Isocontours of constant azimuthal vorticity for $M = 2.46$ and $Re = 30,000$, $\theta = 0°$.

pulse in the recirculation region. Now, as for the $M = 1.2$ case and in contrast to the case with $M = 2.46$ and $Re_D = 25,000$, the disturbances grow exponentially in time (starting at $Re_D = 30,000$), a clear indication of an absolute instability. Figures 6.6 and 6.7 show instantaneous contour lines of total vorticity for $Re_D = 30,000$. It is obvious that the large structures exist; in fact, we found that the intensity (amplitude) of these structures is on the order of 15% of the free stream velocity. Thus, they are at least of the same relative strength as for incompressible wakes.

The qualitative effect of the dynamics of the large structures on the time-averaged base pressure is evident from Figure 6.8. As for the lower Mach number case ($M = 1.2$; see above), the base pressure of the time-averaged
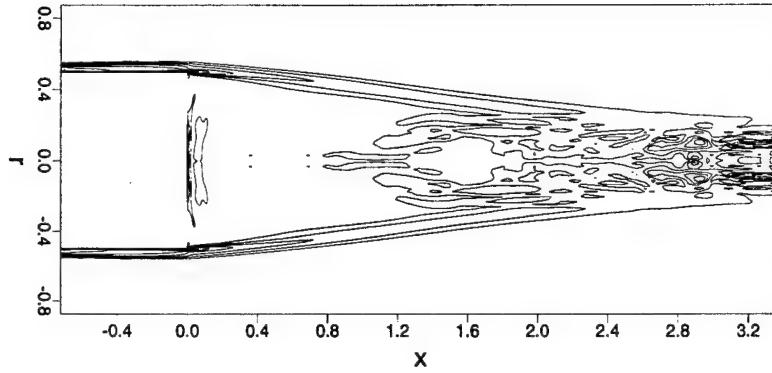
Figure 6.7 Isocontours of constant azimuthal vorticity for $M = 2.46$ and $Re = 30,000$, $\theta = 90°$

flow field has an almost constant distribution over the radius, which is consistent with experimental results. In this case, the effect of base pressure reduction due to the time-dependent structures is even larger than for the lower Mach number case.

For Reynolds number larger than $30,000$ the old fourth-order explicit code required exceedingly costly computations, so all DNS conducted for $Re_D \geq 30,000$ employed the new, higher order code. Figure 6.9 shows color-contours of total vorticity of the plane $\theta = 0°$ for a full 3-D calculation at $Re_D = 100,000$. One can clearly see that the simulation employing the new sixth-order compact difference stencils is able to resolve small scale structures throughout the domain shown. Also, it is important to note that the flow

Figure 6.8 Base pressure distribution for a steady axisymmetric flow field and a time-averaged unsteady flow field for $M = 1.2$ and $Re = 4,000$.

behavior at the points on the axis-line do not appear explicitly in this picture but rather are like at any other point in the field, an indication that the new axis-treatment is working very well.

End-view images of instantaneous total vorticity are displayed in figure 6.10 for different downstream locations. Figure 6.10 a) is a slice very close to the base and shows the small structures in the recirculation zone and no apparent symmetry is present (except that with respect to $\theta = 0°$). At the locations b) and c) which are comparable to locations C and D in Bourdon & Dutton (1998), turbulent structures that have undergone substantial growth can be seen. Also, the presence of longitudinal structures in the shear layer is clearly visible. The position d), which is a cut in the trailing wake and can be compared to position E in Bourdon & Dutton (1998), shows the
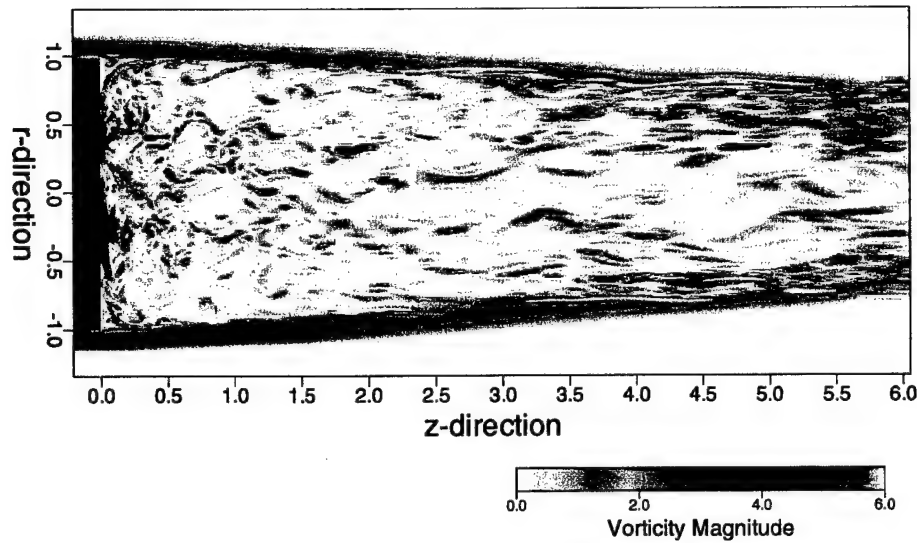
Figure 6.9 Instantaneous color-contours of total vorticity for 3D-DNS; $Re_D = 100,000$; $M = 2.46$; $\theta = 0°$.

formation of a symmetry with respect to $\theta = 90°$ as observed in the experiments. This clearly indicates that even though the Reynolds number chosen for the simulations is an order of magnitude smaller than that in the experiment, qualitative agreement is achieved. Note that all results shown here are instantaneous views of the unsteady flow field.

Figures 6.11 and 6.12 show instantaneous contour lines of total vorticity for $Re_D = 100,000$. Again, it is visible that large structures exist and it is clear that the higher order code resolves more scales than the formerly used fourth-order explicit code. This is also impressively demonstrated in figures 6.13 and 6.14 where instantaneous contours and colour-contours are shown for Mach lines and pressure, respectively. The new code is able to capture the shocklets that occur in the flow, originating from the structures in the
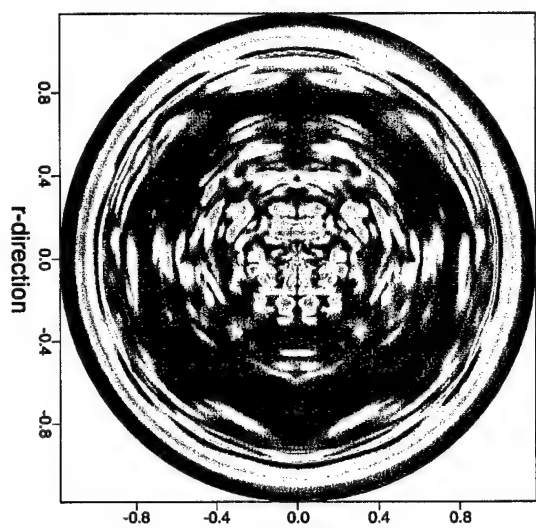
a) z=0.5
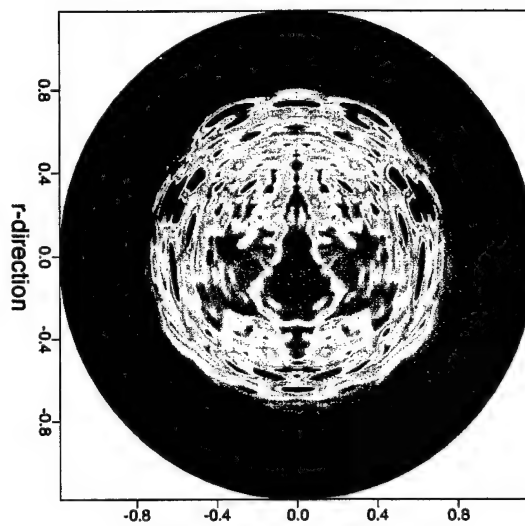
b) z=6
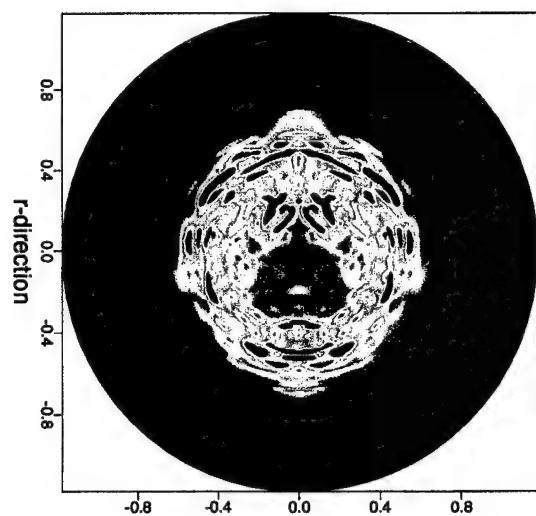
c) z=8
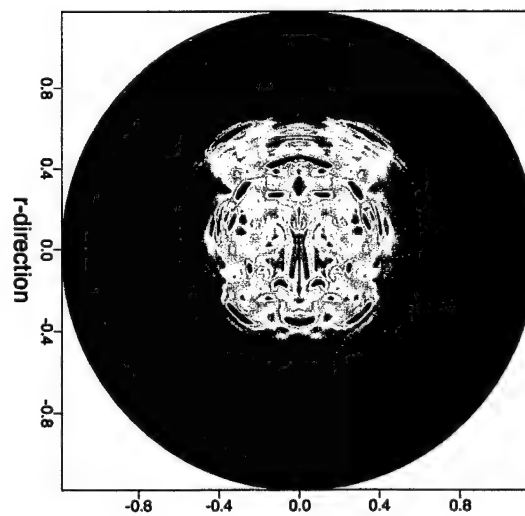
d) z=12

Figure 6.10 Contours of instantaneous total vorticity for various downstream locations; $Re_D = 100,000$; $M = 2.46$.
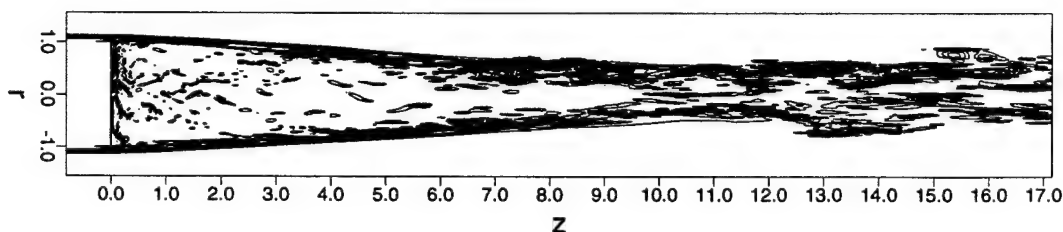
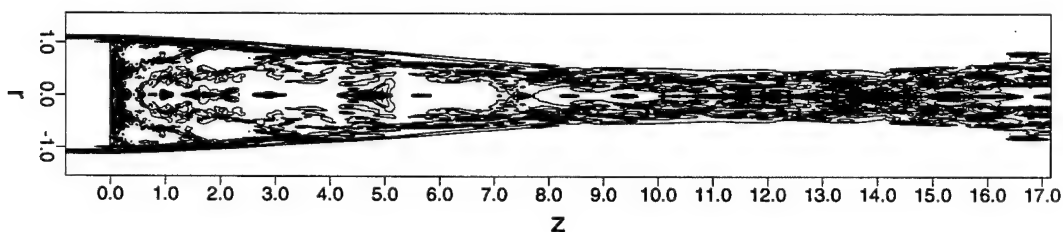Figure 6.11 Isocontours of constant azimuthal vorticity for $M = 2.46$ and $Re = 100,000$, $\theta = 0°$.

Figure 6.12 Isocontours of constant azimuthal vorticity for $M = 2.46$ and $Re = 100,000$, $\theta = 90°$.

shear layer and travelling downstream. Resolving these pressure-gradients is necessary for describing the dynamics of the flow correctly.

Another proof of the existence of large structures was also established in our Direct Numerical Simulations of a two-dimensional base flow for $M = 2.46$ and $Re_D = 250,000$. Typical results from these investigations are shown in Figures 6.15 and 6.16. It is obvious that large structures are present, even when, as in this case (larger Reynolds number), they are resulting from an absolute instability and did not require continuous forcing. The structures are most dynamic in the shear layer (see Figures 6.15 and 6.16), where vortex merging occurs and results in larger, more energetic structures.
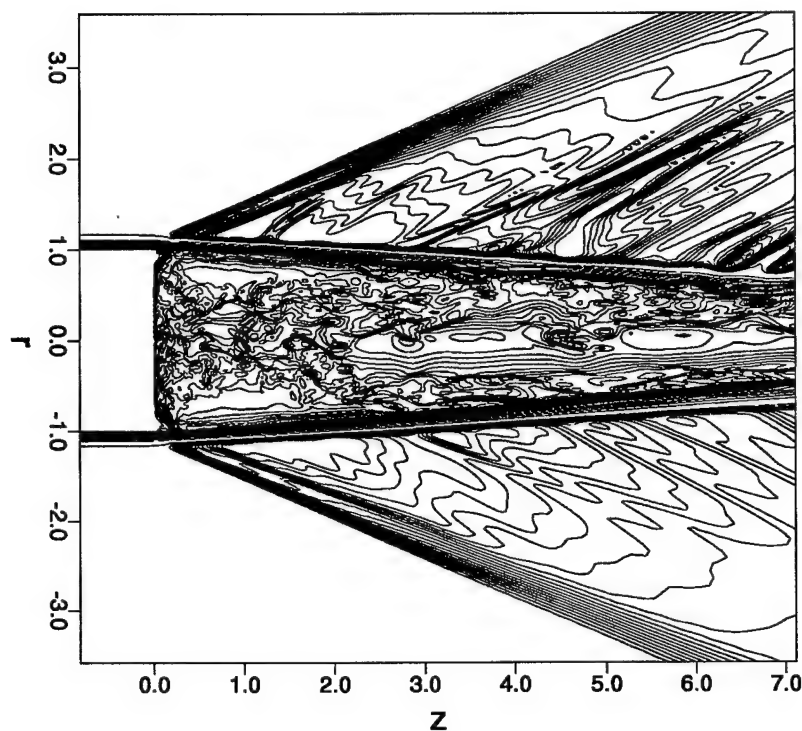
Figure 6.13 Instantaneous contours of Mach lines for 3D-DNS; $Re_D = 100,000$; $M = 2.46$; $\theta = 0°$.
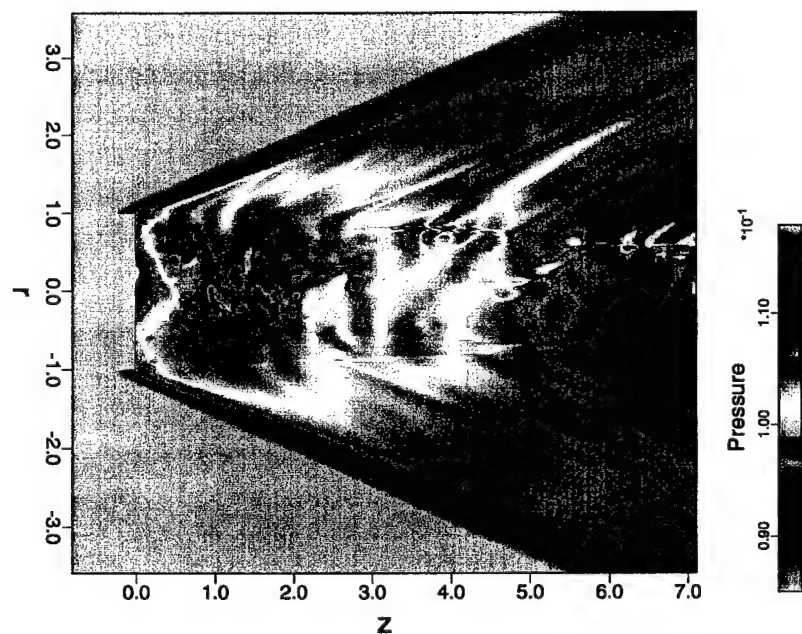

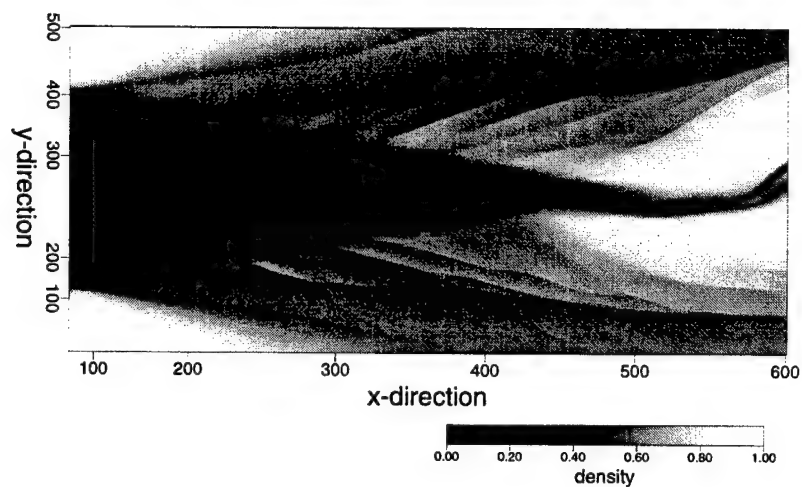Figure 6.14 Instantaneous color-contours of pressure for 3D-DNS; $Re_D = 100,000$; $M = 2.46$; $\theta = 42°$.

Figure 6.15 Contours of instantaneous density for DNS of two-dimensional base flow for $M = 2.46$ and $Re = 250,000$.

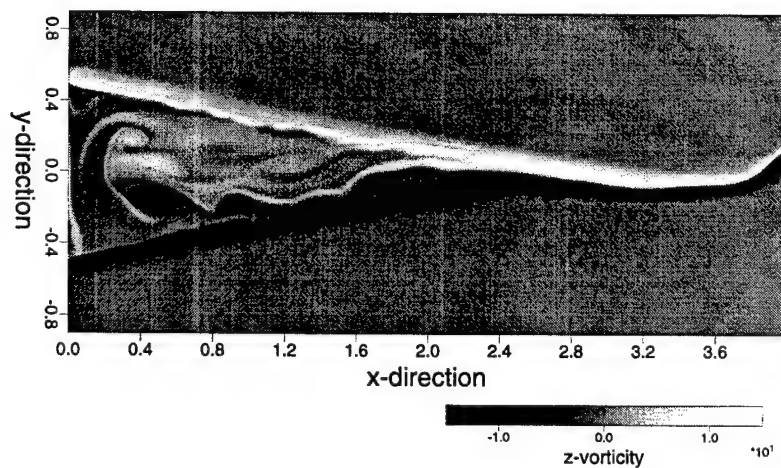Figure 6.16 Contours of instantaneous spanwise vorticity for DNS of two-dimensional base flow for $M = 2.46$ and $Re = 250,000$.

6.2   Large Eddy Simulation

For investigations of higher Reynolds number turbulent flows and as a benchmark for unsteady RANS and FSM calculations, we also implemented subgrid-scale turbulence models for Large-Eddy Simulations (LES). In a first step, we implemented a Smagorinsky-type subgrid-scale turbulence model into our original DNS code. This turbulence model was suggested for compressible flow by Professor C. Speziale of Boston University. With this model, we calculated turbulent wake flows for a range of Reynolds numbers, from transitional all the way to fully turbulent wakes.

In order to test and validate the LES code, we have performed simulations for the same Mach number, $M = 2.46$, as in the experiments carried out at the University of Illinois (Dutton and co-workers). However, the range of Reynolds numbers in our simulations was considerably lower, between 30,000 and 400,000 (based on base diameter). Typical results of LES obtained with the standard fourth-order-accurate code and with the Smagorinsky-type subgrid-scale model (as proposed for compressible flow by C. Speziale) are presented in Figures 6.17 - 6.32 for $M = 2.46$ and Reynolds numbers $Re_D = 30,000$ and 100,000.

Comparison of corresponding plots for Reynolds numbers 30,000 and 100,000 (Figures 6.17 - 6.32) indicates that there are still quantitative and
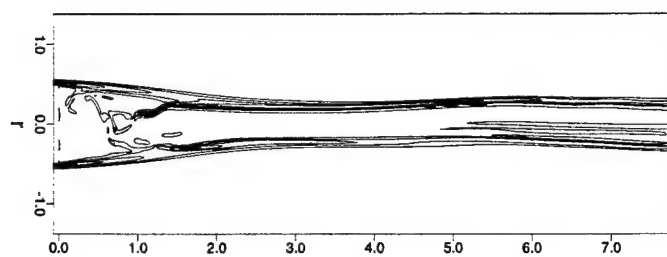
Figure 6.17 Isolines of instantaneous total vorticity from LES with a Smagorinsky model: $M = 2.46$ and $Re = 30,000$.
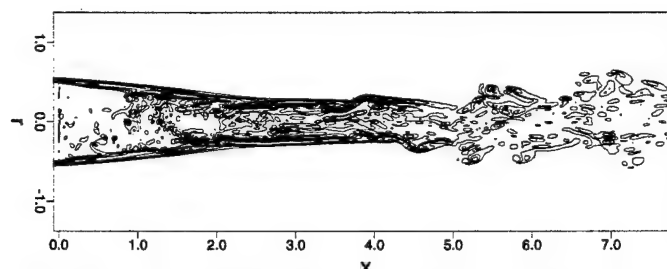

Figure 6.18 Isolines of instantaneous total vorticity from LES with a Smagorinsky model: $M = 2.46$ and $Re = 100,000$.

qualitative changes of the flow field and the turbulent statistics as the Reynolds number increases from 30,000 to 100,000. However, when comparing the results for Reynolds numbers between 100,000 and 400,000 (not shown here), the changes with Reynolds number are not significant, which may be an indication that the accuracy of the code together with the Smagorinsky subgrid-scale model was not sufficient for high-quality simulations that would allow detailed investigation of the flow physics for high Reynolds numbers. This was the motivation for developing the considerably more accurate compact codes and for developing the Flow Simulation Methodology (FSM) (as discussed in 3.5) so that reliable simulations can be performed for considerably higher Reynolds numbers.
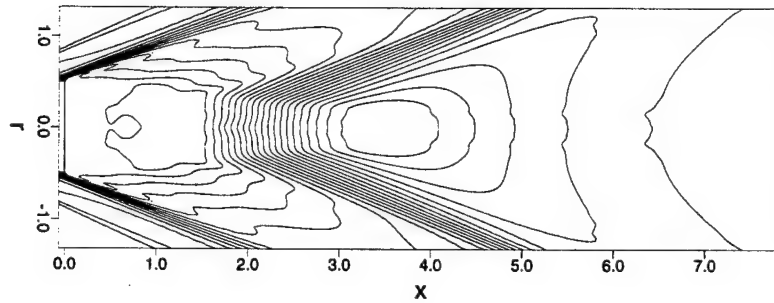
Figure 6.19 Isolines for the time-averaged flow field with $M = 2.46$ and $Re = 30,000$ from LES with a Smagorinsky model: pressure.
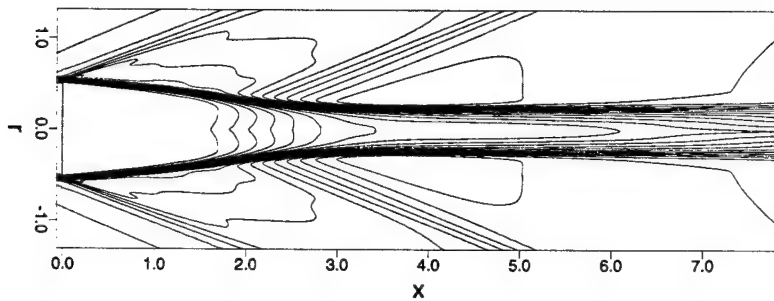

Figure 6.20 Isolines for the time-averaged flow field with $M = 2.46$ and $Re = 30,000$ from LES with a Smagorinsky model: density.
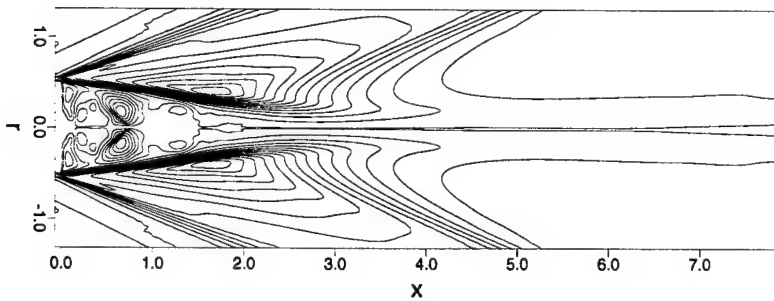

Figure 6.21 Isolines for the time-averaged flow field with $M = 2.46$ and $Re = 30,000$ from LES with a Smagorinsky model: radial velocity.
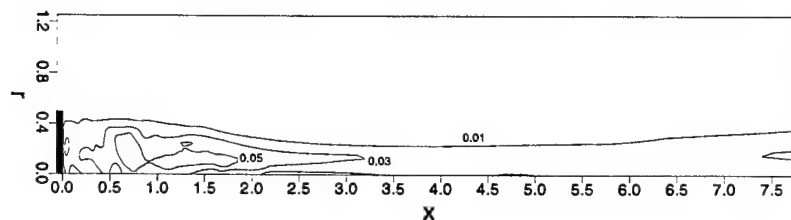
Figure 6.22 Isolines for time-averaged quantities with $M = 2.46$ and $Re = 30,000$ from LES: radial turbulence intensity.
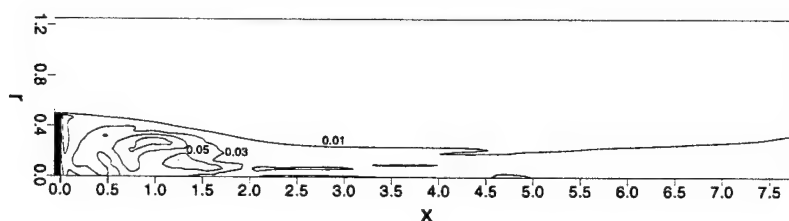

Figure 6.23 Isolines for time-averaged quantities with $M = 2.46$ and $Re = 30,000$ from LES: azimuthal turbulence intensity.
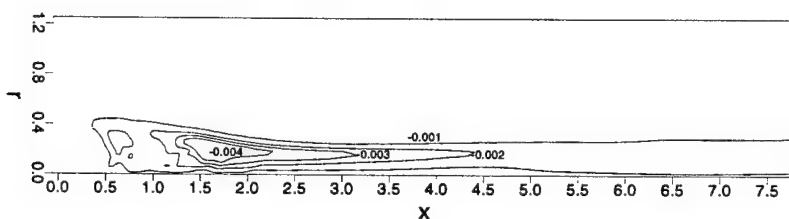

Figure 6.24 Isolines for time-averaged quantities with $M = 2.46$ and $Re = 30,000$ from LES: azimuthal component of turbulent Reynolds stress.
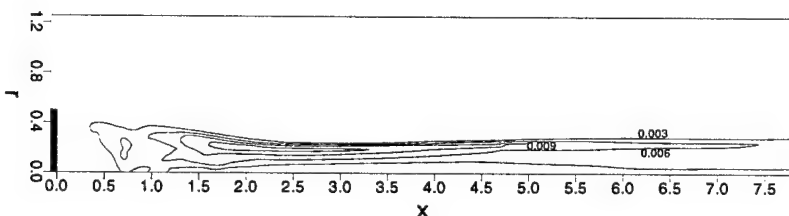

Figure 6.25 Isolines for time-averaged quantities with $M = 2.46$ and $Re = 30,000$ from LES: turbulent kinetic energy.
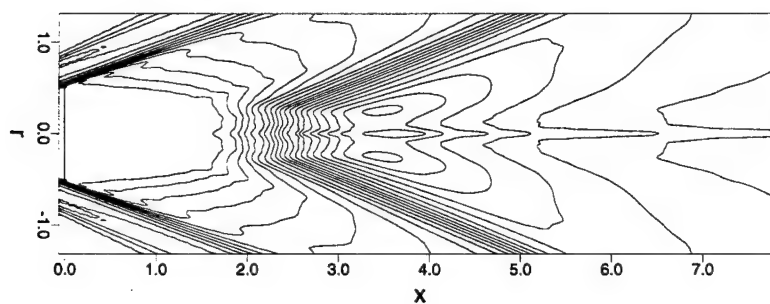
Figure 6.26 Isolines for the time-averaged flow field with $M = 2.46$ and $Re = 100,000$ from LES with a Smagorinsky model: pressure.
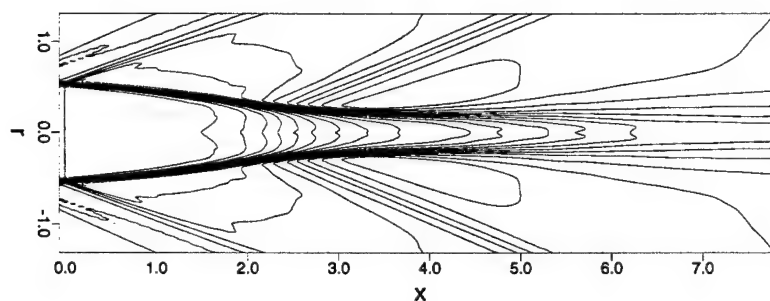

Figure 6.27 Isolines for the time-averaged flow field with $M = 2.46$ and $Re = 100,000$ from LES with a Smagorinsky model: density.
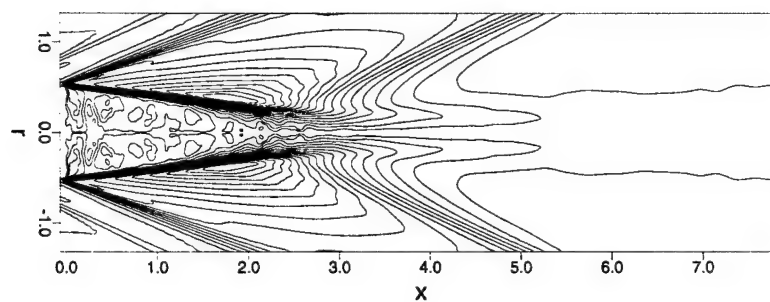

Figure 6.28 Isolines for the time-averaged flow field with $M = 2.46$ and $Re = 100,000$ from LES with a Smagorinsky model: radial velocity.

Figure 6.29 Isolines for time-averaged quantities with $M = 2.46$ and $Re = 100,000$ from LES: radial turbulence intensity.

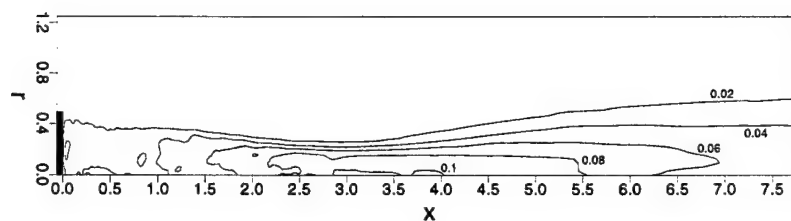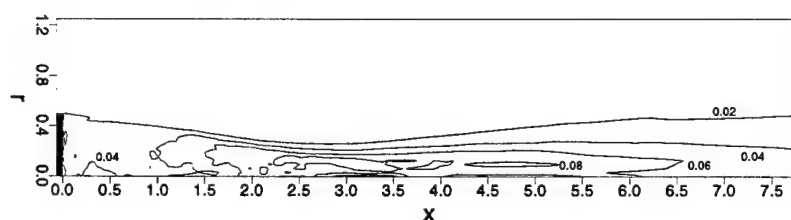Figure 6.30 Isolines for time-averaged quantities with $M = 2.46$ and $Re = 100,000$ from LES: azimuthal turbulence intensity.
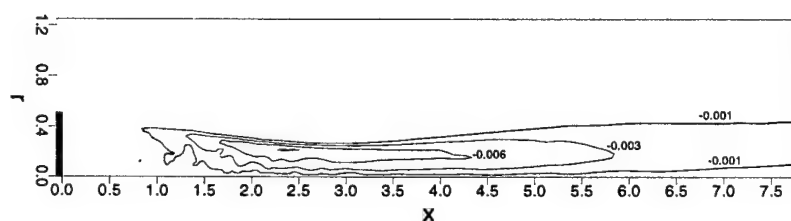

Figure 6.31 Isolines for time-averaged quantities with $M = 2.46$ and $Re = 100,000$ from LES: azimuthal component of turbulent Reynolds stress.
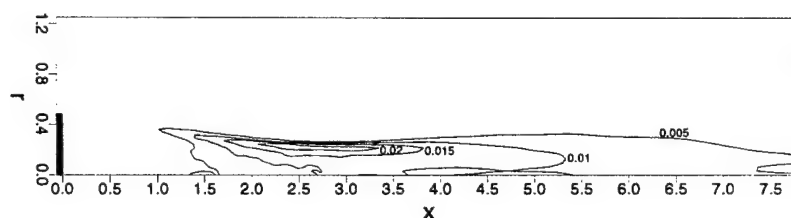

Figure 6.32 Isolines for time-averaged quantities with $M = 2.46$ and $Re = 100,000$ from LES: turbulent kinetic energy.

6.3   Reynolds Averaged Navier Stokes

So far, only 2-D simulations have been performed for the supersonic case by Dutton and co-workers. The initial condition for the supersonic, high Reynolds number cases was the axisymmetric result for $Re_D = 100,000$ and $M = 2.46$ obtained by DNS. In addition, the distribution of K and ε was set to a uniform constant throughout the computational domain. All calculations were performed on a relatively coarse grid with 250 points in the streamwise and 120 points in the radial direction.

Figures 6.33-6.36 show the influence of various inflow boundary conditions for K. When K is kept constant at the inflow (6.33), the turning angle of the shear layer is larger and the recirculation length shorter than if a Neumann condition is used (cases 6.34 and 6.35). This can be explained by the fact that for the ASM model, K and ε vanish in the approach boundary layer if K is not kept at a constant value at the inflow, thus producing a laminar boundary layer that generates unsteady shedding in the shear layer. In case 6.36, the standard $K - \varepsilon$ model produces a more turbulent boundary layer and, consequently, comes closest to the experiments by Dutton and co-workers in terms of turning angle and recirculation length.

Figure 6.33 Color-contours of instantaneous vorticity for 2-D ASM, with Dirichlet condition for K at inflow; $Re_D = 3,300,000$; $M = 2.46$.

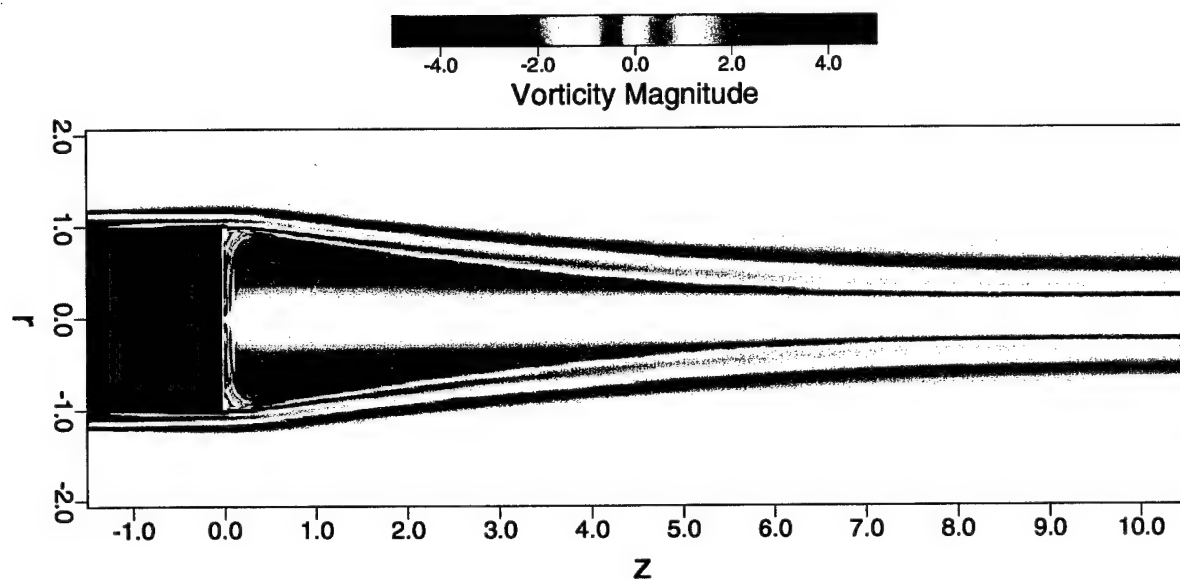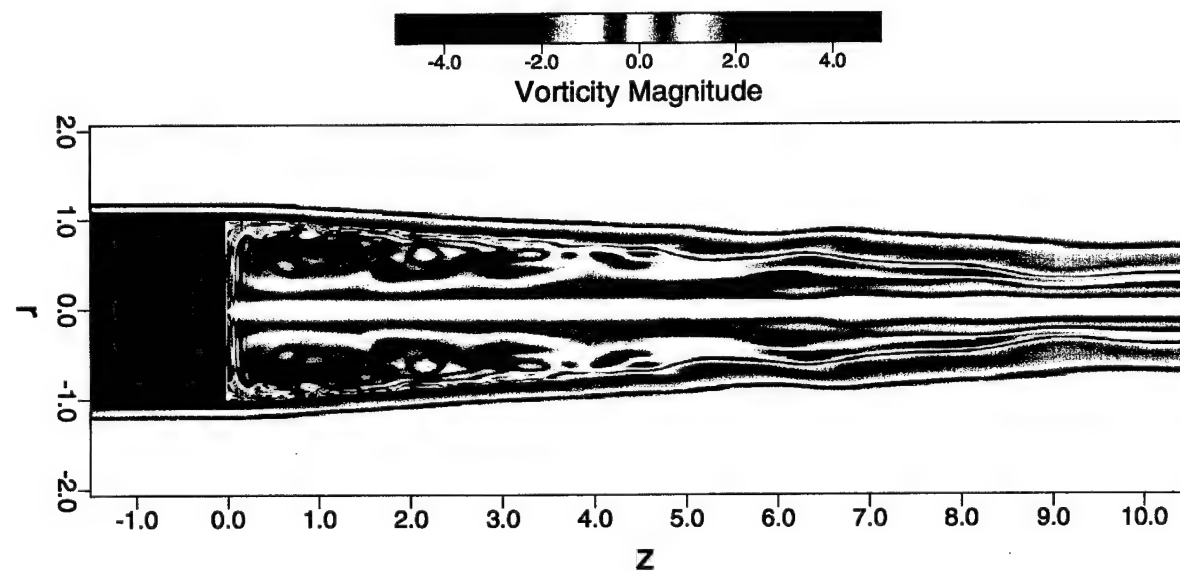Figure 6.34 Color-contours of instantaneous vorticity for 2-D ASM, with Neumann condition for K at inflow; $Re_D = 3,300,000$; $M = 2.46$.
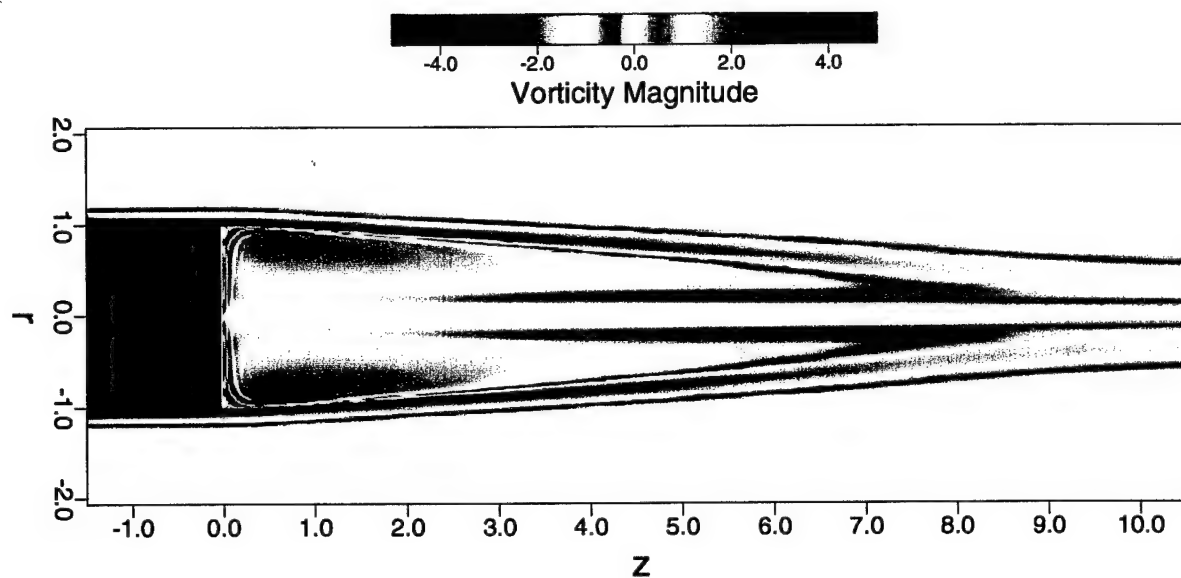
Figure 6.35 Color-contours of averaged vorticity for 2-D ASM, with Neumann condition for K at inflow ; $Re_D = 3,300,000$; $M = 2.46$.
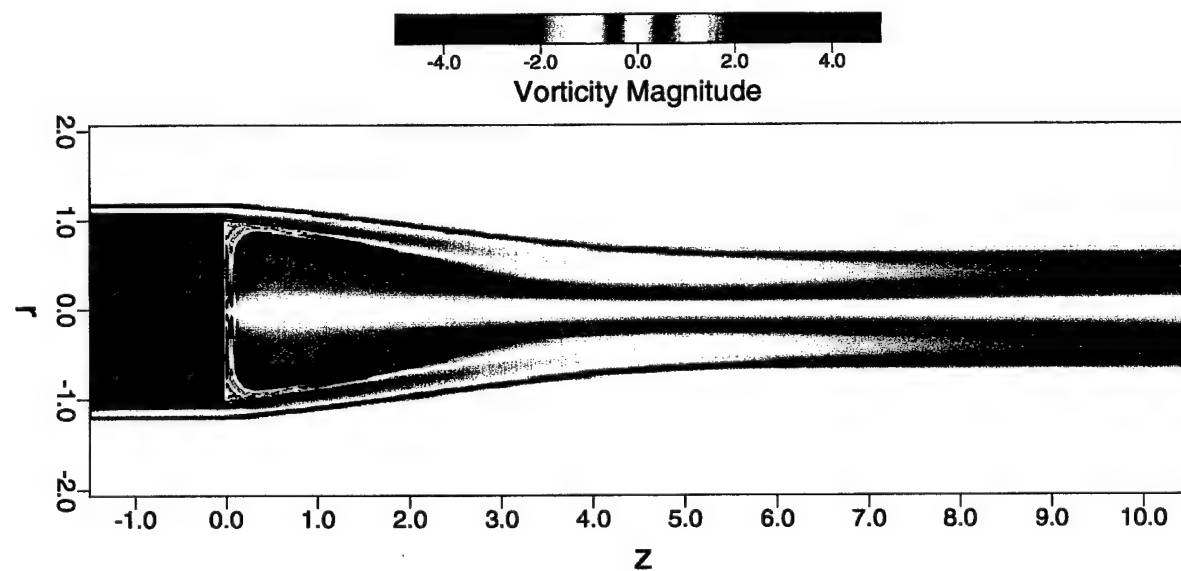

Figure 6.36 Color-contours of instantaneous vorticity for 2-D standard $K-\varepsilon$-model; $Re_D = 3,300,000$; $M = 2.46$.

6.4   Flow Simulation Methodology

Finally, FSM has been applied to the wake-flow, even though so far only in 2-D. Figures 6.37 - 6.40 show color contours of instantaneous vorticity for a test-case at $Re_D = 100,000$ and $M = 0.2$ for a 2-D "DNS", 2-D "FSM" with different β and a 2-D "URANS" calculation, all with a resolution 210x120x1. It is obvious that the amount of dissipation becomes larger for higher contributions of the Reynolds Stresses. In fig.6.37, no turbulence model is used and because of the simulation being 2-dimensional, there is a significant amount of energy trapped in the 2-D mode downstream of the corner.

The strength of that vortex even deforms the shear layer and generates a massive shear layer break-up close to the base ($z \approx 1.5$). For the FSM calculation with $\beta = 0.0001$ shown in fig. 6.38, the instability in the shear layer is damped due to the higher amount of dissipation and the vorticies develop further downstream ($z \approx 2.5$).

The contribution function in this case gave values between 5-25%. For the case of $\beta = 0.002$ and the URANS calculation shown in figures 6.39 and 6.40, respectively, the instantaneous flow field looks very similar, largely because for this value of β and any larger value the contribution of the turbulence model is very large in the whole domain and therefore the RANS-limit is
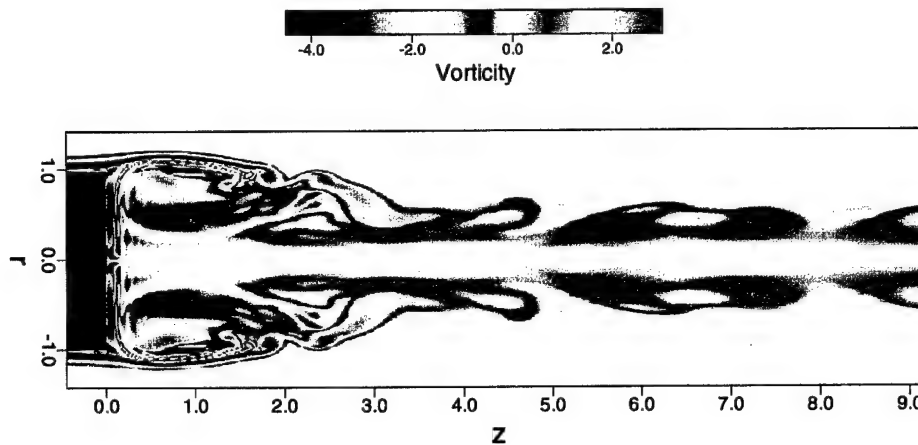
Figure 6.37 Color-contours of instantaneous vorticity for 2-D "DNS"; $Re_D = 100,000$; $M = 0.2$.

approached. In these cases the vorticies develop even further downstream ($z \approx 4.0$) and there is no deformation of the shear layer anymore. However, it is important to note that the simulation still produces these unsteady structures even with the large amount of turbulent dissipation added (no forcing is required to obtain these structures; they arise due to the strong shear layer instability).

Figure 6.38 Color-contours of instantaneous vorticity for 2-D "FSM" with $\beta = 0.0001$; $Re_D = 100,000$; $M = 0.2$.

Figure 6.39 Color-contours of instantaneous vorticity for 2-D "FSM" with $\beta = 0.002$; $Re_D = 100,000$; $M = 0.2$.

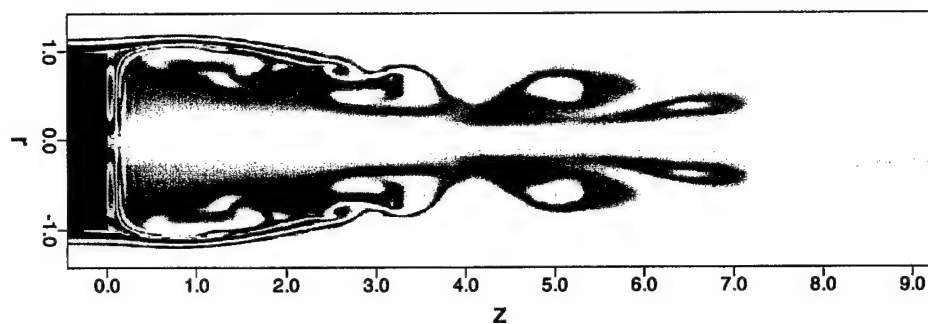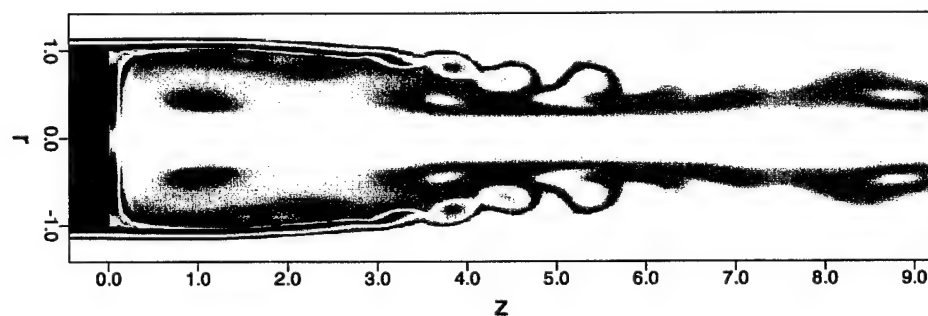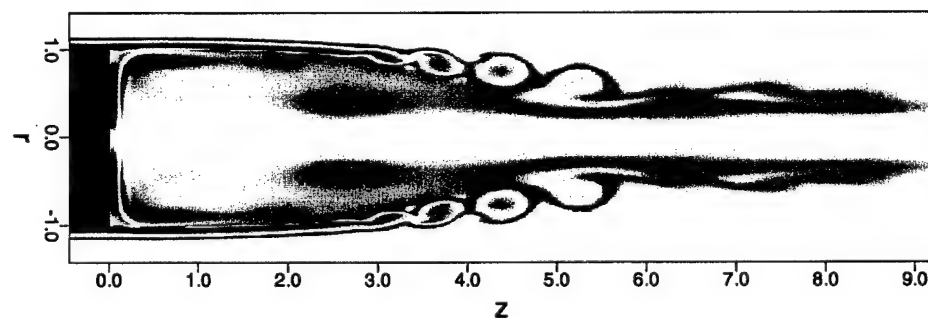Figure 6.40 Color-contours of instantaneous vorticity for 2-D URANS; $Re_D = 100,000$; $M = 0.2$.

7. CONCLUSIONS

For bluff bodies at supersonic speeds, a significant portion of the drag is associated with base drag, caused by the low pressure on the base. This base pressure is greatly influenced by large vortical structures, which, for axisymmetric bodies, are of helical nature. While the vortex formation process and the nature of the helical structures has been studied in depth for incompressible flows, both experimentally and numerically, considerably less is known regarding their information for supersonic flows. Experiments have confirmed the existence of large structures in supersonic flows, but their behavior is poorly understood.

A new, high-order compressible Navier-Stokes code using compact difference stencils of 6th-order accuracy derived for non-equidistant grids and a state-of-the-art axis treatment was developed to investigate the stability behavior in an axisymmetric, bluff body wake at $M = 2.46$. This Mach number was chosen to enable comparison with experiments conducted at the University of Illinois at Urbana Champaign by Dutton and co-workers.

Turbulence models, such as Large Eddy Simulation (LES) and Reynolds Averaged Navier Stokes (RANS) calculations were also incorporated into the code. The $K - \varepsilon$ equations were implemented in fully three-dimensional form to ensure that RANS simulations can capture azimuthal variations in

the flow field (e.g., helical structures).

In particular we have also developed and successfully implemented the new Flow Simulation Methodology (FSM). The centerpiece of FSM is a strategy to provide the proper amount of modeling of the subgrid scales. This is accomplished by a "contribution function" which locally and instantaneously compares the smallest relevant scales to the local grid size. The contribution function is designed such that it provides no modeling if the computation is locally well resolved so that the computation approaches a Direct Numerical Simulation (DNS) in the fine grid limit, or provides modeling of all scales in the coarse grid limit and thus approaches an unsteady RANS (URANS) calculation. In between these resolution limits, the contribution function adjusts the necessary modeling for the unresolved scales while the larger (resolved) scales are computed as in traditional Large Eddy Simulations (LES).

Our calculations have shown that an absolute instability at $M = 1.2$ exists already for $Re_D = 4,000$, however, for $M = 2.46$, the onset of the absolute instability was not observed until $Re_D \geq 30,000$. Preliminary unsteady RANS simulations (URANS) for $Re_D = 3,300,000$ at $M = 2.46$ were performed and showed coherent structures.

All the results obtained so far have shown that the developed Navier Stokes code functions properly and that the high-order compact differencing is of great advantage for supersonic base flow simulations. Furthermore, cal-

culations with the implemented Flow Simulation Methodology (FSM) have demonstrated that this approach has great promise for allowing simulations of supersonic base flows for much larger Reynolds numbers than possible with conventional Large Eddy Simulations.

Bibliography

ANDERSON, D. A., TANNEHILL, J. C. & PLETCHER, R. H. 1984 *Computational Fluid Mechanics and Heat Transfer*. McGraw-Hill.

BOURDON, C. J. & DUTTON, J. C. 1998 Planar visualizations of large-scale turbulent structures in axisymmetric supersonic separated flows. *Phys. Fluids* **11**, 201–213.

BOURDON, C. J. & DUTTON, J. C. 2000*a* Effects of boattailing on the turbulence structure of a compressible base flow. *AIAA Paper* **2000-2312**, 38th aerospace sciences meeting, Reno NV, Jan. 2000.

BOURDON, C. J. & DUTTON, J. C. 2000*b* Shear layer flapping and interface convolution in a separated supersonic flow. *AIAA J.* **38**, 1907.

BOURDON, C. J. & DUTTON, J. C. 2001 Visualizations and measurements of axisymmetric base flows altered by surface disturbances. *AIAA Paper* **2001-0286**, 39th aerospace sciences meeting, Reno NV, Jan. 2001.

BOUSSINESQ, J. 1877 Théorie de l'écoulement tourbillant. *Mem. Pre. par. div. Sav.* **23**.

BOWMAN, W. C. & CLAYDEN, W. A. 1968 Boat-tailed afterbodies at M=2 with gas ejection. *AIAA J.* **2**, 2029.

CANNON, S. & CHAMPAGNE, F. H. 1991 Large-scale structures in wakes behind axisymmetric bodies. In *8th Symposium on turbulent shear flows*.

CHAPMAN, D. R. 1951 An analysis of base pressure at supersonic velocities and comparison with experiments. NACA Rep. 1051. National Advisory Committee for Aeronautics.

CHEN, J., MANSOUR, N. & CANTWELL, B. 1990 The effect of Mach number on the stability of a plane supersonic wake. *Phys. Fluids A* **2**, 984.

CHILDS, R. E. & CARUSO, S. C. 1987 On the accuracy of turbulent base flow predictions. *AIAA Paper* **87-1439**.

CLAYDEN, W. A. & BOWMAN, W. C. 1968 Cylindrical afterbodies at M=2 with hot gas ejection. *AIAA J.* **6**, 2429.

CORTWRIGHT, E. M. & SCHROEDER, A. H. 1951 Preliminary investigation of effectiveness of base bleed in reducing drag of blunt-base bodies in supersonic stream. NACA Rep. RM E51 A26. National Advisory Committee for Aeronautics.

DANBERG, J. & NIETUBICZ, C. 1992 Predicted flight performance of base bleed projectiles. *Journal of Spacecraft and Rockets* **29** (3), 366–372.

DAYMAN, B. 1963 Support interference effect on the supersonic wake. *AIAA J.* **8**, 1921–1923.

DELERY, J. M. & WAGNER, B. 1990 Results of Garteur action group AG09 on flow past missile afterbodies. Symposium on missile aerodynamics, Friedrichshafen, Germany. AGARD/FDP.

DEMETRIADES, A. 1968 Turbulence measurements in an axisymmetric compressible wake. *Phys. Fluids* **11**, 1841–1852.

DING, Z., CHEN, S., LIU, Y., LUO, R. & LI, J. 1992 Wind tunnel study of aerodynamic characteristics of base combustion. *J. Propulsion and Power* **8**, 630.

DONALDSON, I. 1955 The effect of sting supports on the base pressure of a blunt-based body in a supersonic stream. *Aeronautical Quarterly* **6**, 221–229.

DURBIN, P. A. 1993 A Reynolds stress model for near wall turbulence. *J. Fluid Mech.* **249**, 465–498.

DUTTON, J. C. & ADDY, A. L. 1993 Fluid dynamic mechanisms and interactions within separated flows. UILU-ENG 93-4019. University of Illinois at Urbana-Champaign.

FERZIGER, J. H. 1981 *Numerical Methods for Engineering Application*. John Wiley & Sons.

109

FORSYTHE, J. R. & HOFFMANN, K. A. 2000 Detached-eddy simulation of a supersonic axisymmetric base flow with an unstructured solver. *AIAA Paper* **00-2410**, fluids 2000, Denver CO, June 2000.

FORSYTHE, J. R., HOFFMANN, K. A. & SQUIRES, K. D. 2002 Detached-eddy simulation with compressibility corrections applied to a supersonic axisymmetric base flow. *AIAA Paper* **02-0586**.

GATSKI, T. B. & SPEZIALE, C. G. 1993 On explicit algebraic stress models for complex turbulent flows. *J. Fluid Mech.* **254**, 59–78.

HANNEMANN, K. & OERTEL, H. 1989 Numerical simulation of the absolutely and convectively unstable wake. *J. Fluid Mech.* **199**, 55–88.

HARRIS, P. J. & FASEL, H. F. 1996 Numerical investigation of unsteady plane wakes at supersonic speeds. *AIAA Paper* **96-0686**, 34th aerospace sciences meeting and exhibit, Jan 15, 1996 / Reno NV.

HERRIN, J. L. & DUTTON, J. C. 1991 An experimental investigation of the supersonic axisymmetric base flow behind a cylindrical afterbody. UILU 91-4004. University of Illinois at Urbana-Champaign.

HERRIN, J. L. & DUTTON, J. C. 1994 Supersonic base flow experiments in the near wake of a cylindrical afterbody. *AIAA J.* **32** (1), 77.

HERRIN, J. L. & DUTTON, J. C. 1995 Effect of a rapid expansion on the development of compressible free shear layers. *Phys. Fluids* **7** (1), 159–170.

HUBBARTT, J. E., STRAHLE, W. C. & NEALE, D. H. 1981 Mach 3 hydrogen external/base burning. *AIAA J.* **19**, 745.

HUERRE, P. & MONKEWITZ, P. A. 1990 Local and global instabilities in spatially developing flows. *Ann. Rev. Fluid Mech.* **22**, 473–537.

JIMÉNEZ, J. & MOSER, R. D. 1998 LES: where are we and what can we expect. *AIAA Paper* **98–2891**.

MARASLI, B., CHAMPAGNE, F. H. & WYGNANSKI, I. 1989 Modal decomposition of velocity signals in a plane, turbulent wake. *J. Fluid Mech.* **198**, 255.

MATHUR, T. & DUTTON, C. 1996*a* Base-bleed experiments with a cylindrical afterbody in supersonic flow. *Journal of Spacecraft and Rockets* **33**, 30.

MATHUR, T. & DUTTON, C. 1996*b* Velocity and turbulence measurements in a supersonic base flow with mass bleed. *AIAA J.* **34**, 1153.

MEITZ, H. & FASEL, H. F. 2000 A compact-difference scheme for the Navier-Stokes equations in vorticity-velocity formulation. *J. Comp. Phys.* **157**, 371–403.

MORKOVIN, M. V. 1968 Méchanique de la turbulence. In *Centre de la Recherche Scientifique, Paris*, p. 367.

NIETUBICZ, C. & GIBELING, H. 1993 Navier-Stokes computations for a reacting, M864 base bleed projectile. *AIAA Paper* **93-0504**, 31st Aero. sciences meeting and exhibit, Reno / Jan 1993.

OERTEL, H. 1979 Mach wave radiation of hot supersonic jets investigated by means of the shock tube and new optical techniques. Proc. 12th Int. Symp. on shock tubes and waves. Jerusalem.

ORTWERTH, P. J. & SHINE, A. J. 1977 On the scaling of plane turbulent shear layers. *Tech. Rep..* AFWL-TR-77-118.

PAPAMOSCHOU, D. & ROSHKO, A. 1988 The compressible turbulent shear layer: An experimental study. *J. Fluid Mech.* **197**, 453–477.

PETRIE, H. L. & WALKER, B. J. 1985 Comparison of experiment and computations for a missile base region flow field with a centered propulsive jet. *AIAA Paper* **85-1618**.

REID, J. & HASTINGS, R. C. 1959 The effect of a central jet on the base pressure of a cylindrical afterbody in a supersonic stream. Reports and Memoranda 3224. Aeronautical Research Council, Great Britain.

ROLLSTIN, L. 1987 Measurement of inflight base-pressure on an artillery-fired projectile. *AIAA Paper* **87–2427**.

ROSHKO, A. & THOMKE, G. J. 1966 Observations of turbulent reattachment behind an axisymmetric downstream facing step in supersonic flow. *AIAA J.* **4**, 975.

SAHU, J. 1992 Numerical computations of supersonic base flow with special emphasis on turbulence modeling. *AIAA Paper* **92-4352**, AIAA Atmospheric Flight Mechanics Conference, Aug 1992, Hilton Head Island, SC.

SAHU, J. & HEAVEY, K. R. 1995 Numerical investigation of supersonic base flow with base bleed. *AIAA Paper* **95-3459**.

SAHU, J. & NIETUBICZ, C. 1994 Three-dimensional flow calculations for a projectile with standard and dome bases. *Journal of Spacecraft and Rockets* **31**, 103.

SAHU, J., NIETUBICZ, C. & STEGER, J. 1985 Navier-Stokes computations of projectile base flow with and without mass injection. *AIAA J.* **23** (9), 1348–1355.

SANDBERG, R. D. 1999 Investigation of turbulence models for boundary layer flows using temporal numerical simulations. Master's thesis, The University of Arizona.

SARKAR, S. 1992 The pressure-dilatation correlation in compressible flows. *Phys. Fluids A* **4** (12), 2674–2682.

SARKAR, S., ERLEBACHER, G., HUSSAINI, M. Y. & KREISS, H. O. 1991 The analysis and modelling of dilatational terms in compressible turbulence. *J. Fluid Mech.* **227**, 473–493.

SCHWARZ, V., BESTEK, H. & FASEL, H. F. 1994 Numerical simulation of nonlinear waves in the wake of an axisymmetric bluff body. *AIAA-Paper* **94-2285**.

SIEGEL, S. G. 1999 Experimental investigation of the wake behind an axisymmetric body. PhD thesis, The University of Arizona.

SMAGORINSKY, J. 1963 General circulation experiments with the primitive equations. I. The basic experiment. *Mon. Weather Rev.* **91**, 99–164.

SMITH, B. L. & DUTTON, J. 1996 Investigation of large-scale structures in supersonic planar base flows. *AIAA J.* **34**, 1146.

SPALART, P. R., W.-H., J., STRELETS, M. & ALLMARAS, S. R. 1997 Comments on the feasibility of LES for wings, and on a hybrid RANS/LES approach. In *Advances in DNS/LES, 1st AFOSR Int. Conf. on DNS/LES, Aug 4-8, 1997*. Greyden Press, Columbus, OH.

SPEZIALE, C. G. 1997 A combined large-eddy simulation and time-dependent RANS capability for high-speed compressible flows. *Tech. Rep.* AM-97-022. Boston University.

SPEZIALE, C. G. 1998 Turbulence modeling for time-dependent RANS and VLES: A review. *AIAA J.* **36, 2**, 173–184.

SPEZIALE, C. G. & SO, R. M. C. 1996 Turbulence modeling and simulation. Handbook of Fluid Dynamics Ch. 9. Boston University.

STUREK, W. & NIETUBICZ, C. 1992 Recent applications of cfd to the aerodynamics of army projectiles at the u.s. army ballistic research laboratory. *AIAA Paper* **92-4349**, aIAA Atmospheric Flight Mechanics Conference, Aug 1992, Hilton Head Island, SC.

TERZI, D. A. v. & FASEL, H. F. 2002 A new flow simulation methodology applied to the turbulent backward-facing step. *AIAA Paper* **2002–0429**, 40th aerospace sciences meeting and exhibit, Reno / Jan 2002.

THOMPSON, K. W. 1987 Time dependent boundary conditions for hyperbolic systems. *J. Comp. Phys.* **68**, 1–24.

THUMM, A. 1991 Numerische untersuchungen zum laminar-turbulenten strömungsumschlag in transsonischen grenzschichtströmungen. PhD thesis, Universität Stuttgart.

TOURBIER, D. 1996 Numerical investigation of transitional and turbulent axisymmetric wakes at supersonic speeds. PhD thesis, The University of Arizona.

TOURBIER, D. & FASEL, H. F. 1994 Numerical investigation of transitional axisymmetric wakes at supersonic speeds. *AIAA Paper* **94-2286**.

VALENTINE, D. & PRZIREMBEL, C. 1970 Turbulent axisymmetric near-wake at Mach four with base injection. *AIAA J.* **8** (12), 2279–2280.

WHITE, F. M. 1991 *Viscous Fluid Flow*. McGraw Hill.

WILCOX, D. C. 1998 *Turbulence Modeling for CFD*, 2nd edn. DCW Industries.

WYGNANSKI, I., CHAMPAGNE, F. H. & MARASLI, B. 1986 On large-scale coherent structures in two-dimensional, turbulent wakes. *J. Fluid Mech.* **168**, 31.

ZHANG, H. L., BACHMAN, C. R. & FASEL, H. F. 2000 Application of a new methodology for simulations of complex turbulent flows. *AIAA Paper* **2000-2535**.